

AUSTENITE-FERRITE INTERFACE MOBILITY IN PURE IRON

A MOLECULAR DYNAMICS STUDY OF
AUSTENITE-FERRITE INTERFACE MOBILITY IN PURE IRON

BY

HUAJING SONG

B.Eng

SEP 2011

A THESIS

SUBMITTED TO THE DEPARTMENT OF MATERIAL SCIENCE AND ENGINEERING

AND THE COMMITTEE ON GRADUATE STUDIES

OF MCMASTER UNIVERSITY

IN PARTIAL FULFILLMENT OF THE REQUIREMENTS

FOR THE DEGREE OF

MASTER OF APPLIED SCIENCE

© Copyright 2011 by Huajing Song, B. Eng. (Material)

All right Reserved

MASTER OF APPLIED SCIENCE (2011)
(Material Science and Engineering)

McMaster University
Hamilton, Ontario

TITLE: A Molecular Dynamics Study of Austenite-Ferrite
Interface Mobility in Pure Fe

AUTHOR: Huajing Song, B. Eng. (Material)

SUPERVISOR: Dr. Jeff. J. Hoyt

NUMBER OF PAGES: ix, 93

Abstract

Molecular dynamics (MD) simulations performed on two-phase simulation cells were used to compute the Austenite (FCC) / Ferrite (BCC) boundary mobility in pure iron (Fe) over the temperature range of 600K - 1400K. An embedded atom method interatomic potential was used to model Fe and the driving force for interface motion is the free energy difference between the two phases, which was computed as a function of temperature using a thermodynamic integration technique. For low index FCC/BCC crystallographic orientations, no interface motion was observed. But for slight misorientations steps were introduced at the interphase and sufficient mobility was observed over MD time scales. A new interphase mechanism was found that instead of the moving of structure disconnection by diffusion control, growing of misfit dislocations in each steps were observed (interphase control). The interphase velocity could reach 2 m/s and the mobility at 1000K was approximately 0.001 mol-m/J-s. In agreement with previous MD studies of grain boundary mobility, we found that the activation energy for the austenite-ferrite boundary mobility was much lower than the values found from previous experiments.

Acknowledgments

I give a sincere gratitude to the people who do engineering with pure unselfish and honest passion as they are the people who make me grow and appreciate the world in the way I see.

I am heartily thankful to my supervisor, Dr. Jeff. J. Hoyt, whose encouragement, guidance and support from the initial to the final level enabled me to develop a comprehensive understanding of the subject and bring me laughters and tears during the project. My colleagues in the Computational Material Science Group, H. Humadi, M.J. Rahman, S. Yasmin and my roommate Dr. Ko have always assisted me in many ways. I would like to thank them for their great company when disasters strike. I also would like to express my gratitude to the graduate students, faculty, administrative and technical members in the Department of Material Science and Engineering at McMaster University for their assistance during my study and research. In addition, I wish to acknowledge the defence committees Dr. Purdy and Dr. Niewczas. Finally, I thanks NSERC for their financial support to our Strategic Project “Bridging the Gap: A New Generation Process Model for Steels by Modeling across Different Length Scales”.

Members of my family and many more than I can include here, have loved me far beyond what I can ever return. I will start by thanking my parents and my sister for their love and continuous support. I would like to thank my girlfriend for her continuous trust and confidence in me. Lastly, I offer my regards and blessings to all of those who supported me in any aspects during the completion of the project.

Table of Contents

Chapter 1	1
Introduction	1
1.1 Transformation kinetics	2
1.2 Interface mobility model	2
1.3 Thesis organization.....	3
Chapter 2	4
General Theory	4
2.1 The iron FCC to BCC transformation	5
2.1.1 Martensitic transformation	5
2.1.2 Massive transformation	6
2.2 Dislocations and Disconnections.....	7
2.2.1 Interface Dislocations	8
2.2.2 Disconnection	9
2.3 Nishiyama-Wasserman and Kurdjumow-Sachs crystallographic relationship	11
2.4 Molecular dynamics simulations (MD).....	16
2.4.1 Isenthalpic ensemble (NPH).....	18
2.4.2 Canonical ensemble (NVT).....	18
2.4.3 Isothermal-Isobaric (NPT) ensemble	19
2.5 The Lennard – Jones (L-J) and Finnis-Sinclair embedded atom method formalism (EAM-fs)	19
2.6 The choice of potential	22
Chapter 3	25
Previous work	25
3.1 Experimental research	25

3.2 Simulation area	31
Chapter 4	33
Approach	33
4.1 Melting temperature	34
4.2 Driving force and lattice parameter	38
4.3 Simulation settings	43
4.3.1 Interface	43
4.3.2 System dimension	45
4.3.3 Equilibrate the system	47
Chapter 5	49
Results: interface velocity, mobility and activation energy	49
5.1.1 Low temperature case (600K & 800K)	52
5.1.2. Normal transformation temperature 1000K and 1200 K	54
5.1.3 High temperature 1400K	56
5.2 Interface velocity, mobility and activation energy	58
5.2.1 Interface velocity	58
5.2.2 Mobility	59
5.2.3 Activation energy and pre-exponential factor M_0	60
5.3 Results and discussion	61
5.4 Summary	65
Chapter 6	66
Interface atomic mechanisms	66
6.1 Determine the interface	66
6.2 Planar interface growth and step ledge growth	69
6.3 Planar secondary disconnection growth	73
6.3.1 Misfit dislocation in the terrace plane	73
6.3.2 Secondary disconnection formation and growth in terrace plane	75
6.4 Analysis and discussion	77

6.5 Summary.....	79
Chapter 7	80
Future research	80
Chapter 8	82
Conclusion.....	82
Appendix A	83
Classical Mechanics of MD simulation.....	83
Appendix B.....	86
Ackland et al. 1997[15] EAM Finnis-Sinclair potential	86
Bibliography	88

List of Figures

Figure 1. Dislocations and Burgers vector	9
Figure 2. Disconnection and Burgers vector	11
Figure 3. Coordinate of K-S & N-W relationship	13
Figure 4. Coherent interface in K-S & N-W relationship	14
Figure 5. N-W FCC/BCC interface ledges.....	15
Figure 6. MD simulation algorithm.....	17
Figure 7. L-J potential profile.....	20
Figure 8. Comparison of Ackland, Mendeleev and L-J iron potential.....	23
Figure 9. Summary of experiment mobility data 1.....	26
Figure 10. Summary of experiment mobility data 2.....	28
Figure 11. Transformation curve for $\gamma \rightarrow \alpha$ in Fe.....	29
Figure 12. C. Bos's simulation box.....	32
Figure 13. FCC coexisting system.....	36
Figure 14. NPH temperature profile.....	36
Figure 15. Potential energy porfile for equilibrating BCC phase.....	39
Figure 16. Free energy graph for FCC and BCC phase	42
Figure 17. 2D view of the simulation box.....	44
Figure 18. Strain vectors of disconnection structure	45
Figure 19. Sketch of the simulation box setting.....	46
Figure 20. 3D schematic of the whole simulation box	48
Figure 21. $\gamma \rightarrow \alpha$ transformation process.....	51
Figure 22. The potential energy Vs simulation time graph for 600 K	53
Figure 23. The potential energy Vs simulation time graph for 800 K	54
Figure 24. The potential energy Vs simulation time graph for 1000 K	55
Figure 25. The potential energy Vs simulation time graph for 1200 K	55
Figure 26. The potential energy Vs simulation time graph for 1400 K	57
Figure 27. The natural logarithm of the mobility graph.....	60

Figure 28. Comparison of the transformation potential energy graph in 5 temperatures..	62
Figure 29. The CS number profile for 1400 K	68
Figure 30. Illustration of a single step disconnection.....	70
Figure 31. HRTEM image showing interfacial disconnections	71
Figure 32. Primary disconnection of FCC-BCC interface	72
Figure 33. Cross section view of the interface in the ideal initial state.....	74
Figure 34. 3D cross section view of the interface during the transformation	76
Figure 35. Potential energy profile of two individual layers of atoms.....	78

List of Table

Table 1. Lattice parameter and potential energy for BCC and FCC phases.....	39
Table 2. Enthalpy of liquid and solid (FCC & BCC) states of iron	40
Table 3. Melting temperature and potential energy function for FCC and BCC	41
Table 4. Dimension and orientation of BCC and FCC phase boxes	47
Table 5. Driving force, interface velocity, and mobility	60
Table 6. Comparison of massive, martensitic and diffuse control phase transformation..	64
Table 7. Real lattice spacing in FCC and BCC phases.....	73

Chapter 1

Introduction

The kinetics of phase transformation in metallic alloys has been studied extensively, especially the transformations that are governed by the long-range diffusion of alloying element and interface mobility. It has long been a generally accepted assumption that diffusional phase transformations appear under local equilibrium at the migrating interface [1]. On the other hand, the massive transformation is participating at the initial moment (before the concentration gradient emerges) and it is accepted that its rate is controlled by the mobility of the interface. Although a general insight into the kinetics of these phase transformations has been developed, observations of the actual atomic processes take place at the interface during the transformation are still very scarce. Since the speed of the interface movement is very fast, no experimental technique is capable of observing the atomic motion that taking place during this phenomenon. Therefore, there remains a largely unanswered question on the fundamental character of the austenite – ferrite transformation. This question is not only of scientific interest, but also of great practical importance for martensite formation in steel and in shape-memory alloys. At present, simulation by means of molecular dynamics (MD) seems to be one of the very few methods available to acquire information about the nature of the austenite – ferrite transformation. Since the transformation is very fast, the actual transformation time can be covered in an MD timescale (0.001ps ~ 1000ns). The growth kinetics will be outlined in Section 1.1 and the basic model of massive transformation will be discussed in Section 1.2. Finally, the organization of this thesis is provided in Section 1.3.

1.1 Transformation kinetics

In the literature, the growth kinetics of pro-eutectoid ferrite formation in Fe alloys is often modeled assuming thermodynamic equilibrium conditions at the α/γ interphase boundary, also known as the local-equilibrium assumption [2]. Therefore, the volume diffusion velocity of the impurity is rate limiting for the growth kinetics. The growth kinetics is then said to be diffusion controlled. The other extreme in modeling the $\gamma - \alpha$ phase transformation is to assume an infinitely fast diffusion of impurity in austenite. In other words, the long-range diffusion effect is ignored in the γ phase. The growth is governed by the rate at which Austenite (FCC) iron transforms into Ferrite (BCC) iron, which is reflected in the intrinsic mobility of the interface. The growth kinetics is then called the interface controlled. In reality, the force created by the diffusion of the solute atoms and the migrating interfaces are always combined together. It thus will be difficult to estimate the reaction of the two forces individually. Therefore, the fundamental atomistic mechanisms and characters of the pure interface controlled transformation are poorly understood. In this thesis, the MD method is used to simulate the austenite to ferrite ($\gamma - \alpha$) phase transformation for pure iron (Fe) to avoid the effect of long-range diffusion. Using this method, a detail image of the interfaces controlled transformation can be created. With all the information, one can gain a deeper understanding on the initial state of the $\gamma - \alpha$ phase transformation, before the solute concentration gradients occur in the γ phase. Future researches like martensitic transformation and diffusion control transformation can be conducted

1.2 Interface mobility model

During the austenite – ferrite transformation, the transformation rate is controlled by the interface mobility, which is usually defined as the constant of proportionality in the rate equation:

$$v = M \times \Delta G_m \quad (1)$$

In Eq.1, v identifies the velocity of the interface, which is the average speed of the atoms when rearranging from Austenite (FCC) lattice to ferrite (BCC) lattice. ΔG_m is the net driving force per mole of the growing phase. It is obvious that the mobility of the interface M is related to these two factors. Therefore, the way to determine the interface's velocity for a given driving force for calculating the mobility is the key point of this research. On the other hand, the driving force for the transformation is the free energy difference between the α and γ phases. It is very important that the free energy difference has to be identified before starting any simulations. For this research, the embedded atom method has been used as the interatomic potential for pure Fe. Based on the method and theory discussed below, the interface's mobility and free energy difference determined in the simulation should be a function of temperature. The activation energy for the mobility can be calculated from the results at different temperatures.

1.3 Thesis organization

This thesis presents a new method to research the austenite to ferrite phase transformation of pure iron. The remainder of the thesis is organized as follows. Chapter 2 gives a description of massive transformation; introduces molecular dynamics and the embedded atom method. In addition, the Nishiyama – Wasserman (NW) crystallographic relationship and the grain boundary defect disconnection will also be illustrated in Chapter 2. Chapter 3 provides a review of previous works concerning the Austenite to Ferrite transformation. Both experimental and simulation-based works will be discussed in detail in this chapter. Chapter 4 elaborates the parameters such as the selected potential energy, the interface relationship and boundary condition of the simulation system used in this research. Chapter 5 discusses the detailed method for tracking and calculating the interface velocity, mobility and activation energy. Chapter 6 focuses on analyzing the interface atomic mechanisms. Finally, the suggestions for further work and conclusion are given in Chapter 7 and Chapter 8 respectively.

Chapter 2

General Theory

The background knowledge and general theory, which are used in this research, will be discussed in this chapter. The iron Austenite to Ferrite transformation means the transformation from the FCC (γ) phase to the BCC (α) phase (2.1). There are two modalities for this transformation: the martensitic transformation (2.1.1) and massive transformation (2.1.2). The objective of this research is to use computer simulation techniques to investigate the massive transformation process in pure iron, study its mechanism and identify the interface mobility and activation energy. Due to the difference of the lattices parameters, a steps structure is applied to connect the FCC and BCC phases and create both the interface dislocation (2.2.1) and disconnection (2.2.2). The closed pack interface relationship, named Nishiyama-Wasserman (NW) and Kurdjumow-Sachs (KS) relationship (2.3) are related to our interface orientation and used to connect the FCC and BCC phases. Chapter 2.4 will introduce the Molecular Dynamics (MD) method, which is selected to simulate the transformation process. Under the MD method, three ensembles: microcanonical ensemble (NVE) (2.4.1), canonical (NVT) (2.4.2) and isothermal-isobaric ensemble (NPT) (2.4.3) are used to control the pressure, temperature, volume and the number of atoms in the structure. In this research, we use the Embedded atom method (EAM) (2.5) to identify the interatomic energy. After comparing several iron potentials (2.6), the Fe-Cu potential presented by Ackland et al. 1997 [15] is selected for our EAM method.

2.1 The iron FCC to BCC transformation

There are at least four allotropic forms of iron, known as α , γ , δ , and ϵ . ϵ is a hexagonal close-packed (HCP) structure, which exists under high temperature and high pressure condition. In this research, we will not be discussing this special phase of iron. At 1 atm pressure and up to a temperature of 1184 K pure iron has the body centered cubic (BCC) crystal structure also known as Ferrite (α). Between 1184 K and 1665 K, iron exists in the face centered cubic (FCC) structure, which is called Austenite (γ). From 1665 K to its melting point, again it has the BCC structure. During this project, the focus is on the transformation from metastable FCC to BCC at low temperature range (600 K – 1200 K).

Two transformation mechanisms: massive and martensitic transformations can be studied with in the embedded atom method (EAM) molecular dynamics simulation time frame. Since the MD method can only simulate the atomic behaviors in the short time frame from 0.001 picoseconds up to several hundreds of nanoseconds, long-range diffusion is not feasible using MD method.

2.1.1 Martensitic transformation

The Martensitic transformation is a diffusion-less transformation, which always occurs in the quenching process for alloy. During the transformation, the movement of a single atom is less than one interatomic spacing. Therefore, during the transformation, the atoms have to move in a coordinated fashion. One of the difference between martensite and austenite is that martensite has a body-centered tetragonal (BCT) structure, whereas austenite has a face-centered cubic (FCC) structure. Besides, martensite has a lower density than austenite, so the martensitic transformation results in a relative change of volume [3]. Because of the incongruent volume change from BCT to FCC, it creates the shear strain, which has a magnitude of about 0.26 and determines the shape of the plates of martensite. The volume change also explains why the martensitic transformation will

create a shear of the atom structure. In the transformation, the interface velocity can reach the speed of sound in the solid. The rapid transformation speed is independent of thermal activation. Since the high transformation speeds make experimental observations difficult, the exact mechanism of this transformation is still not completely understood. Some of the previous researches will be discussed in Chapter 3, but the martensitic transformation is not the focus area of this study.

2.1.2 Massive transformation

The Massive transformation is a composition-invariant nucleation-and-growth formation of a solid phase from another solid phase [1]. In this research, the atomic structure during the transformation for pure iron is studied. In iron, BCC grains tend to nucleate on grain boundaries. This grain growth during transformation requires a larger driving force: the Gibbs free energy difference between the FCC and BCC phases. The growth speed, or the interface velocity is completely determined by the free energy difference and the interface mobility. The interface mobility depends on how easily the atoms can cross the interphase boundary. In order to cross the interphase boundary, an atom has to gain enough energy by thermal fluctuations to overcome the activation energy Q associated with detaching from the FCC lattice and attaching to the BCC lattice. If the interface velocity v is assumed to be proportional to the free energy difference ΔG [1], it can be written as

$$\bar{v} = \bar{M}_0 \exp\left(-\frac{Q}{RT}\right) \Delta G \quad (2)$$

Where M_0 is the pre-exponential factor of mobility, R is the gas constant and T is the temperature. According to J.W. Christian [38], the value of the pre-exponential factor M_0 can also be written in from of

$$\bar{M}_0 = \frac{k\bar{\chi}}{hR} \quad (3)$$

In which, h and k are the Planck and Boltzmann constant respectively, χ is the local displacement of the interface due to the crossing of one iron atom, and R is the gas constant. M_0 can also be seen as an adjustable parameter. In order to obtain the activation energy Q , a range of mobility M in different temperatures have to be identified. Eq.1 shows that the mobility M relates to the transformation speed v and the driving force ΔG at a given temperature. Therefore, the way to identify the velocity v and ΔG is the focus of this research and will be discussed in detail in Chapter 4.

Based on the research from Asta and Hoyt et al [6], a method, which monitored the total potential energy of the system as a function of simulation time, is used to extract the velocity of the solid-liquid interface in solidification of Ni. The same idea could be used in solid-solid interface in massive transformation of iron. As shown in Eq.4

$$v = -\frac{1}{2a\Omega L} \frac{dE}{dt} \quad (4)$$

where a is the area of the interface, L is the latent heat, which in this case is the potential energy difference (per atom value) and Ω is the volume per atom in the FCC phase. The first derivative of the potential energy $\frac{dE}{dt}$ is the average slope of the function potential energy versus simulation time, which can be obtained directly from LAMMPS ("Large-scale Atomic/Molecular Massively Parallel Simulator") [6]. Therefore, the interface velocity can be estimated from this information.

2.2 Dislocations and Disconnections

A dislocation is a kind of crystallographic defect or irregularity, which is first proposed by Vito Volterra in 1905. Formally, dislocation can be defined in terms of the Burgers circuit and described by the Burgers vector \mathbf{b} . Ledges on free surfaces are topologically connected with dislocation and adding a perfect surface onto an equivalent one containing a right-angled ledge creates a pure edge dislocation. Steps with ledge-like

character can also exist at internal interfaces. In the remaining parts of this thesis, we will use ledge for free surfaces and steps for internal interfaces to distinguish between the two cases. From recent researches, several examples showed a new kind of defects with both the pure step character and the pure dislocation character. Because these defects have partial dislocation and a partial step character, it is neither a pure dislocation nor a pure step. These defects are named disconnections by J.P.Hirth (1994) [19].

2.2.1 Interface Dislocations

In materials science, a dislocation is a crystallographic defect or irregularity, which commonly exists in grain boundary and free surface. Burgers vectors are the most prevalent method to identify these defects. Both circuit procedures and the symmetry/dichromatic complex methods [20] for determining Burgers vectors are discussed by Pond and Hirth [19]. In this research, all of the initial dislocations are presented in the FCC – BCC interface. These interface dislocations are created by the misfit defect, which is caused by the lattice parameters difference between the FCC and BCC phase. Figure 1 shows a misfitting surface for a crystal. In Figure 1, α and β are two crystal structures with different lattice parameters, which can be considered as the FCC and BCC atomic structure. They build up an incommensurate interface. Figure 1(b) represents the crystals strained to the coherent or commensurate state. A Burgers circuit is drawn in Figure 1(c) showing an unstrained reference state of the crystal structure. This condition is considered to release all the coherency force on the interface as shown in Figure 1(b). For this case, the Burgers vector is the minimum size dislocation of the dichromatic structures [19], i.e. the superposition of the α and β lattices. The coherency strain can be removed by superposing a misfit dislocation with Burgers vector that has equal magnitude and opposite directions to that of the coherency dislocation as illustrated in Figure 1(d). Under the same idea, the strain also can exist by combining two opposite direction dislocations, as shown in Figure 1(e). In this case, the Burgers circuit can still be used to determine its Burgers vector.

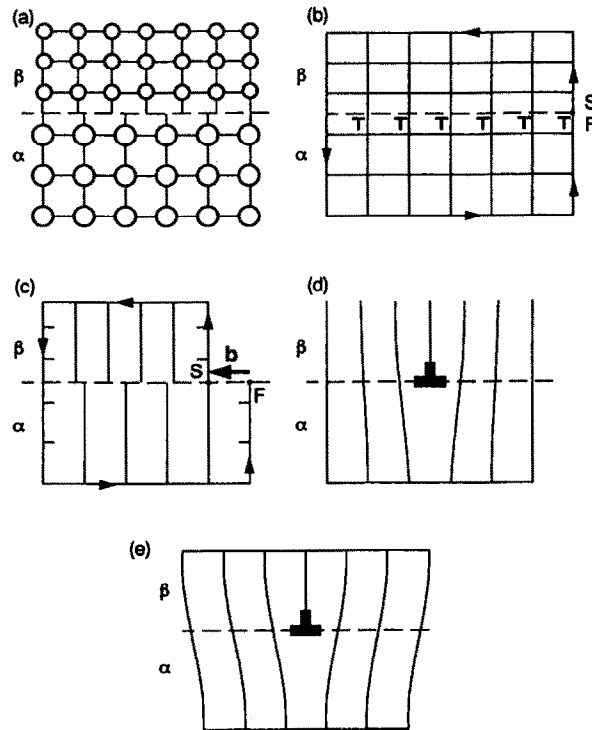


Figure 1. [19]

(a). Incommensurate interface in crystal; (b) Relating strained to lattice parameter of α ; (c) Relaxed reference of (b) and Burgers circuit; (d) Lattice of (b) relaxed in presence of misfit dislocation; (e) Lattice of (d) with both phases strained to normal lattice parameter of a .

2.2.2 Disconnection

Disconnection is another kind of crystallographic defect caused by the mismatch of crystal orientation or lattice parameter on the ledge structure. As illustrated in Figure 2(a), to form a disconnection we consider connecting two crystals with opposing ledge directions. In Figure 2, the crystal surface with a smaller lattice parameter (β) as the terrace plane is shown [19]. The vector \mathbf{n} is normal to the terrace surface, and a step is identified as positive if the step translates the terrace in the direction of \mathbf{n} . \mathbf{l} is the ledge translation vector, which can either be normal or have some angle to the terrace surface. Therefore, the step height h can be determined as $h = \mathbf{n} \cdot \mathbf{l}$. In order to form a disconnection, the two sides of the crystal structure have to have at least one of the differences in lattice parameters, namely atom types or orientations. Otherwise, the

connection will form a single crystal without any defect. Figure 2(a), (b) and (c) show a diverse lattice parameter example. The ledge translation vectors \mathbf{l}_α and \mathbf{l}_β are normal to the terrace surface, which mean the ledge heights h_α is equal to $|\mathbf{l}_\alpha|$ and h_β is equal to $|\mathbf{l}_\beta|$. The crystals are rigidly brought into contact in Figure 2(b). Since the lattice parameter for the two sides are different ($\mathbf{l}_\alpha \neq \mathbf{l}_\beta$), it must leave a gap to the right of the step. Then the gap is closed by intermolecular forces and creates a disconnection. This disconnection has both step characters (the contact region in Figure 2(b)), and dislocation characters (arising from the gap closure). Here, the Burgers vector \mathbf{b} and the step translation vector \mathbf{l} of the disconnections are respectively:

$$\vec{b} = \vec{l}_\alpha + \vec{l}_\beta \quad (5)$$

$$\vec{l}_\alpha = -\vec{l}_\beta \quad (6)$$

Figure 2. (d) – (f) illustrate a less simple step formation. In this case, the ledge vector \mathbf{l}_β is inclined to the terrace normal of β , so the ledge height is the projected length ($h = \mathbf{n} \cdot \mathbf{l}$). In order to close the gap in Figure 2(e), atom displacements need to be both parallel and perpendicular to the interface. As a consequence, the disconnection has both components $\mathbf{b}_1=h$ and $\mathbf{b}_2=m$, which are horizontal and vertical to the terrace plane. The Burgers vector is the net vector of \mathbf{b}_1 and \mathbf{b}_2 , which can be calculated by Eq.5. In general, a component \mathbf{b}_3 can be presented in the 3-dimensions case; more interface defect analysis will be discussed in Chapter 6.2.

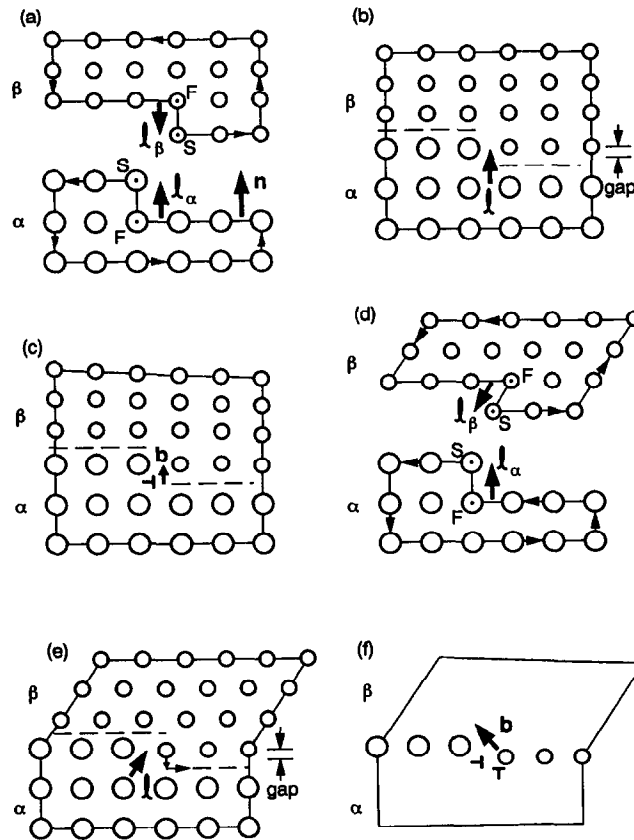


Figure 2. [19]

(a) crystals of α and β with ledges; (b) crystals in (a) rigidly brought into contact; (c) relaxed version of (b); (d) crystals of α and β with ledges; (e) crystals in (c) rigidly brought into contact; (f) relaxed version of (e).

2.3 Nishiyama-Wasserman and Kurdjumow-Sachs crystallographic relationship

Most of the transmission electron microscope (TEM) investigations demonstrate that FCC austenite and BCC ferrite has huge mismatch even under the crystallographic condition specified by the experimentally determined conjugate habit planes and lattice orientation relationship. The critical length requirement to consider a tiny defect as a

misfit dislocation is very small when compared with the mismatch between the FCC and BCC lattices. Therefore, the defect commonly exists in the interface. The mismatch and resulting elastic strain energy is too large to permit the existence of a misfit dislocation structure and to create an essentially disordered boundary [30].

In order to reduce the mismatch strain energy, a special interface orientation is required to match up as many atoms as possible. Therefore, two superposition interface relationships were proposed in this projection. They are the Nishiyama-Wasserman (N-W) relationship and the Kurdjumow-Sachs (K-S) relationship and are described as follows:

Nishiyama-Wasserman (N-W): $(110)_{bcc} // (111)_{fcc}$ and $[001]_{bcc} // [1\bar{1}0]_{fcc}$

Kurdjumow-Sachs (K-S): $(110)_{bcc} // (111)_{fcc}$ and $[1\bar{1}1]_{bcc} // [1\bar{1}0]_{fcc}$

Both of these relationships have the closest packed planes in each phase in contact $\{111\}_{fcc} // \{110\}_{bcc}$, but N-W has a 5.26° rotation about the plane normal. Figure 3 shows the rhombic unit cells difference between the K-S and N-W orientation. In this figure, each corner of the rhombic represents an atom in the K-S or N-W system. Figure 3 assumes the atom A is overlapping in both K-S and N-W relationship and setting up two 2-D coordinates (x, y) and (x', y') . The (x, y) coordinate is employed for the K-S system and CB $[111]_{bcc}$ is parallel to QP $[1\bar{1}0]_{fcc}$, and coordinate (x', y') is applied to the N-W system. If the CA $[001]_{bcc}$ is parallel to AQ $[011]_{fcc}$, Figure 3 will be converted to a N-W orientation. Therefore, if $\angle(\beta-\alpha)=0^\circ$, the system identifies the N-W relationship. On the other hand, if $\angle(\beta-\alpha)=5.26^\circ$, it denotes the K-S relationship.

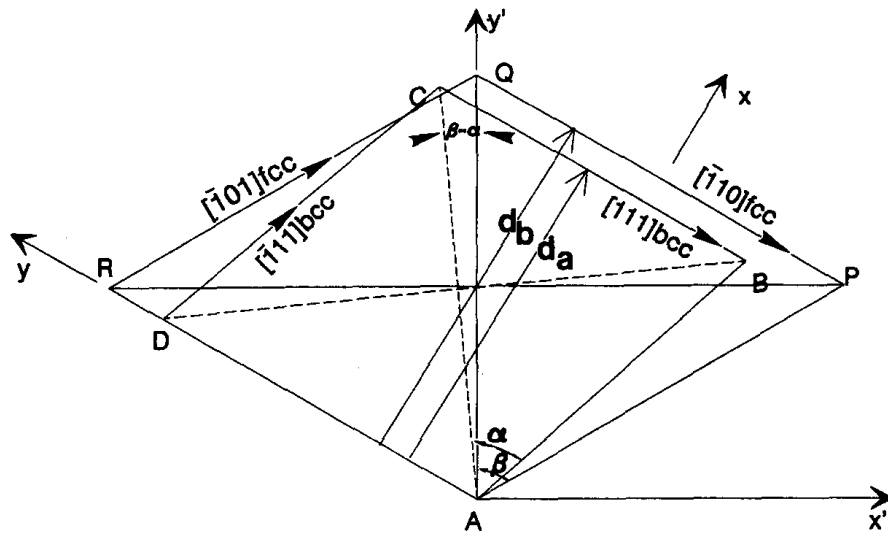


Figure.3 [31]

A unit cell shows the relation between the Kurdjumov-Sachs (K-S) and Nishiyama-Wassermann (N-W) orientation. ABCD for $\{110\}_{bcc}$ and APQR for $\{111\}_{fcc}$. Coordinate (x', y') is applied for the N-W system and (x, y) coordinate is employed for the K-S system. The angle $\angle(\beta-\alpha)=5.26^\circ$ discriminate the two relationships.

Hall et al. [32] reported that even with a chosen close-packed interface relationship, only 8% of the atoms in the interphase boundary should be regarded as coherent as depicted in Figure 4. The coherent atoms were found to be grouped into small regions whose sizes and distributions were sensitive to the precise rotation of the parallel planes $\{111\}_{fcc}$ and $\{110\}_{bcc}$. Therefore, a huge strain exists on the interface because of the misfit dislocation in the system. Hall et al is still trying to find a better method to connect these two phases in order to reduce the interface strain.

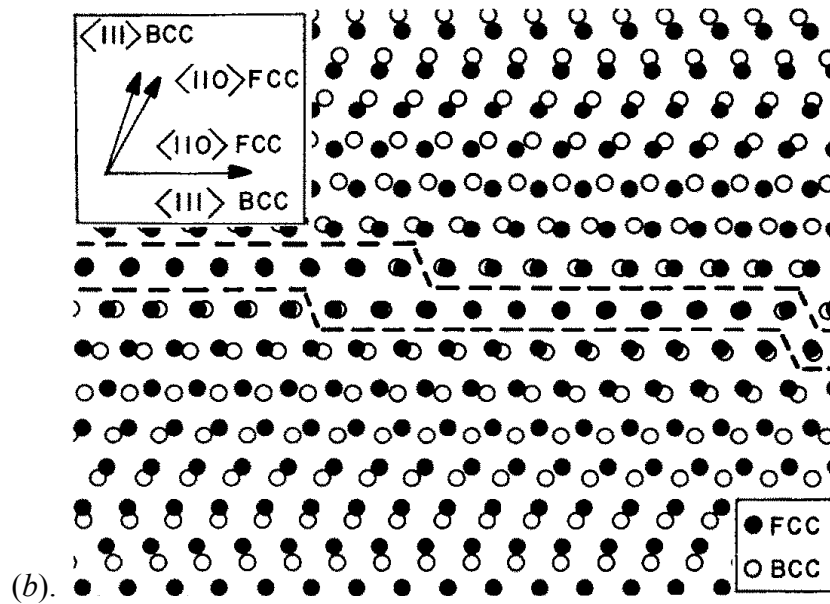
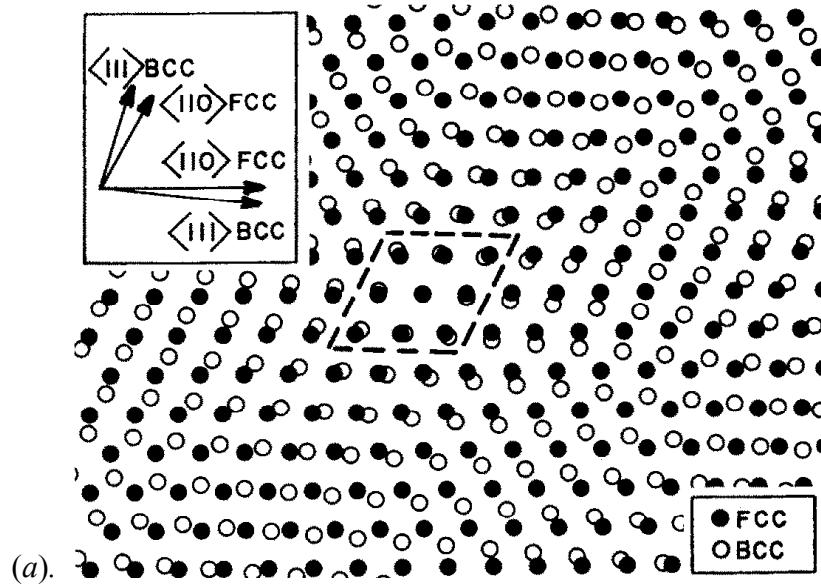


Figure.4 [32]

Superposed plots of the atomic configurations in the $\{111\}_{fcc}$ and $\{110\}_{bcc}$ planes.

(a) Nishiyama-Wasserman orientation relationship.

(b) Kurdjumov-Sachs orientation relationship.

Based on their research, Hall et al also found that the insertion of monatomic ledges between coherent regions in the FCC/BCC boundary increased the frequency of repetition of these regions and raised the proportion of coherent atom in the boundary to around 25%. As shown in Figure 5, the ledges increase the repeating frequency of these matching regions in the interface by creating a N-W relationship in each step. More detail about these step structures can be found in Chapter 4.

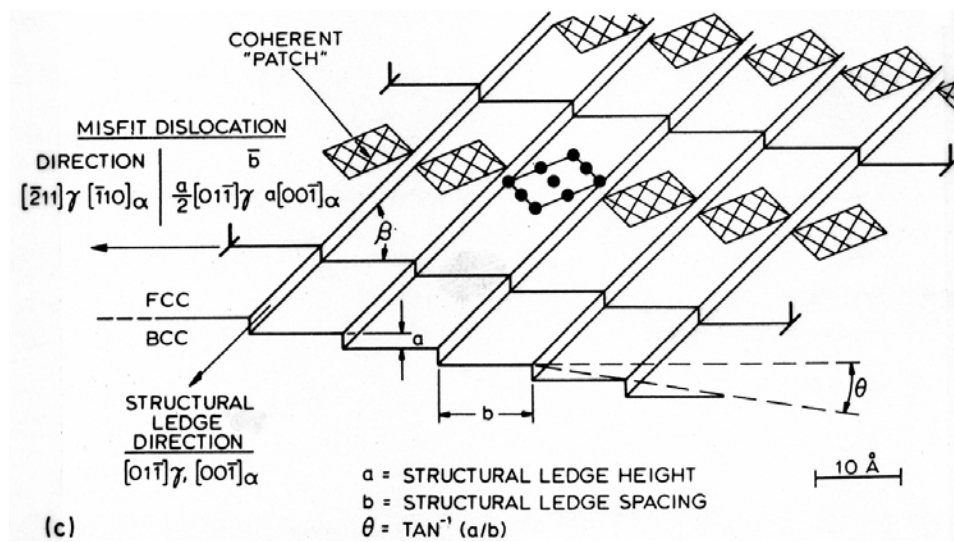


Figure.5 [30]

A Nishiyama-Wasserman oriented fcc/bcc interface with structure ledges and misfit dislocation

2.4 Molecular dynamics simulations (MD)

The molecular dynamics simulation method is based on Newton's second law or the equation of motion, $\mathbf{F} = m \times \mathbf{a}$, where \mathbf{F} is the force vector exerted on the particle, m is its mass and \mathbf{a} is its acceleration. From knowledge of the force on each atom, it is possible to determine the acceleration of each atom in the system. Integration of the equations of motion then yields a trajectory that describes the positions, velocities and accelerations of the particles as they vary with time. From this trajectory, the average values of properties can be determined. This method is deterministic; once the positions and velocities of each atom are known, the state of the system can be predicted at any time instant.

As shown in Eq.7.

$$\vec{a}_i = \frac{\vec{F}_i}{m_i} \quad (7)$$

with

$$\vec{F}_i = -\sum_j \nabla \phi_{ij} \quad (8)$$

where \mathbf{F}_i denotes the force acting on atom i , and ϕ is the interatomic potential energy. Therefore, the force \mathbf{F}_i is the sum of potential energies acting on atom i by a distance over all its neighbor atom j . a_i is the acceleration of atom i and m_i is the mass of atom i , with the index i running over all atoms in the system. All the information needed by these equations include an initial list of atomic positions and velocities, and a model of the atomic interactions with which ϕ can be calculated given the positions r_i .

One frequent source of confusion is the meaning of temperature in MD. Commonly we have experienced with macroscopic temperatures, which involve a huge number of particles. But temperature is a statistical quantity. If there are a large enough

number of atoms, statistical temperature can be estimated from the instantaneous temperature, which is found by equating the kinetic energy of the system to $nk_B T/2$ where n is the number of degrees of freedom of the system. A temperature-related phenomenon arises due to the small number of atoms that are used in MD simulations. For example, consider simulating the growth of a copper film starting with a substrate containing 500 atoms and a deposition energy of 100 eV. In reality, the 100 eV from the deposited atom would rapidly be transported through and shared among a large number of atoms (10^{10} or more) with no big changes in temperature. When there are only 500 atoms, however, the substrate is almost immediately vaporized by the deposition. Therefore, a large system that contains more than 10^6 of atoms should be used to avoid the temperature effect during the transformation.

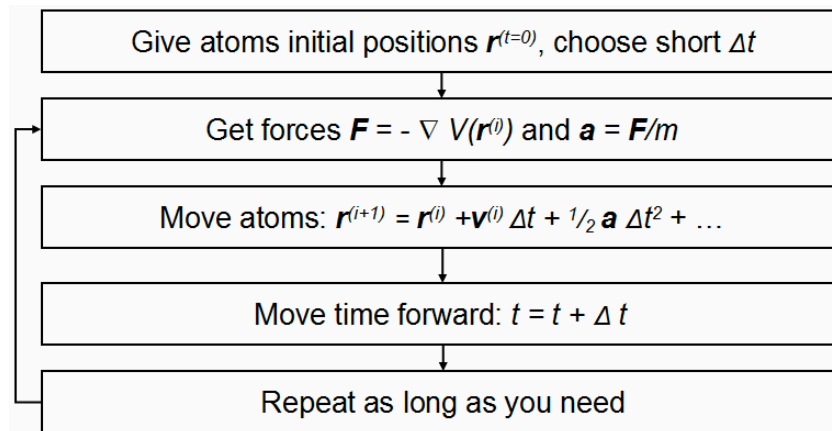


Figure 6

Figure 6 shows a highly simplified description of the molecular dynamics simulation algorithm. The simulation proceeds iteratively by alternatively calculating forces and solving the equations of motion based on the accelerations obtained from the new forces. In practise, almost all MD codes use much more complicated versions of the algorithm that including two steps (predictor and corrector) in solving the equations of motion and many additional steps for e.g. temperature, volume and pressure control, analysis and output. The following sections 2.4.1 ~ 2.4.3 will discuss some of these algorithms which are going to be used in this studying.

2.4.1 Isenthalpic ensemble (NPH)

In the isenthalpic, or NPH ensemble, the system is isolated from changes in moles (N), pressure (P) and enthalpy (H). Enthalpy is a measurement of the total energy of a thermodynamic system. Therefore, this ensemble corresponds to a process with no energy exchange with the environment. A microcanonical molecular dynamics trajectory may be seen as an exchange of potential and kinetic energy, with total energy being conserved. For a system of N particles with coordinates X and velocities V , the first order differential equations may be written in Newton's notation Eq.7 & 8. The temperature of the system in NPH is naturally raised due to the latent heat generation during the melting of metal such as iron in this research. In the NPH ensemble simulates the condition, only the exchange of potential and kinetic energy and no energy transmits in or out of the system. This ensemble can be used to stabilize the solid – liquid interface and identify the melting point as will be detailed in Chapter 4.

2.4.2 Canonical ensemble (NVT)

In the canonical ensemble, moles (N), volume (V) and temperature (T) are conserved. It is also called constant temperature molecular dynamics (CTMD). In NVT, the energy of endothermic and exothermic processes is exchanged with a thermostat. A variety of thermostat methods are available to add and remove energy of an MD system in a more or less realistic way, approximating the canonical ensemble. It is a popular technique to control temperature includes velocity rescaling. The ensemble is not trivial to obtain a canonical distribution of conformations and velocities using these algorithms. On one hand, this ensemble fixes the box volume, boundary and temperature, which is advantageous to maintain the atomic framework and avoids the shearing and twisting of the structure caused by the initial stress. On the other hand, the atoms in the box can vibrate and adjust the distance between each other. Therefore, NVT ensemble is commonly used during equilibrium step, as will be discussed in section 4.3.3.

2.4.3 Isothermal-Isobaric (NPT) ensemble

In the isothermal-isobaric ensemble, moles (N), pressure (P) and temperature (T) are conserved. In addition to a thermostat, a barostat is needed. It corresponds more closely to laboratory conditions with a flask open to ambient temperature and pressure. NPT ensemble is commonly used in the system equilibrium step. During equilibrium, the system is first under going NVT ensemble to limit the huge vibration of the atoms, and then NPT ensemble with 0 pressure is used to let the system adjust its box dimension to release all the external pressure. Besides, NPT pressure controls not only occur under constant membrane area (NPAT) but also constant surface tension "gamma" ($NP_\gamma T$). $NP_\gamma T$ means only applies pressure controls and boundaries movement in the γ direction (could be single or multi dimensions) but fixes the boundaries in other direction. In order to avoid the external pressure effect on the simulation result, $NP_\gamma T$ ensemble with 0 pressure in the direction perpendicular to the interphase is used during the transformation step in our simulation.

Readers interested in the numerical algorithms used to solve the equations of motions (algorithms that make the atoms move) are referred to Appendix A.

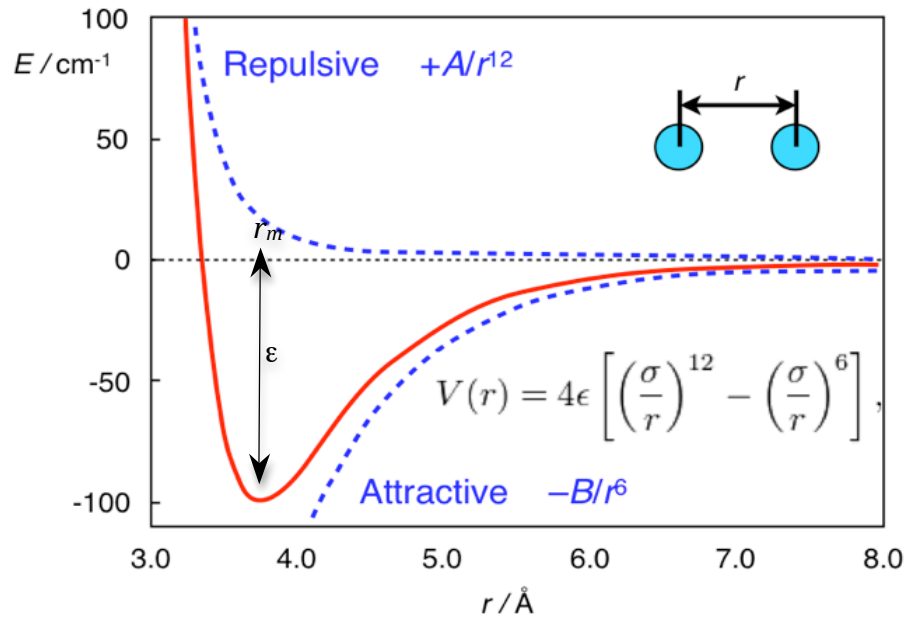
2.5 The Lennard – Jones (L-J) and Finnis-Sinclair embedded atom method formalism (EAM-fs)

In MD simulation, Lennard – Jones and embedded atom method are two of the potential theory; both are mainly applied to simulating the metal behavior. Lennard-Jones potential [39] (also known as L-J potential or 6-12 potential) was first proposed by John Lennard-Jones in 1924. L-J potential is a mathematical approximation model that describes the interaction between a pair of neutral atoms or molecules. As shown in the Eq.9, the potential energy of an atom V_{LJ} is the combination of the repulsive force and

attractive force acting on this atom. r represents the distance between two atoms. The r^{-12} term, which is the repulsive term, describes the repulsion at short ranges due to overlapping electron orbitals and the r^{-6} term, which is the attractive long-range term, describes the long ranges attraction. σ is the cut off distance at which the interatomic potential is far enough to be considered as zero.

$$V_{LJ} = 4\epsilon \left\{ \left(\frac{\sigma}{r} \right)^{12} - \left(\frac{\sigma}{r} \right)^6 \right\} \quad (9)$$

Figure 7 is a sketch of a L-J potential graph. In the figure, ϵ is the depth of the potential well, and r_m is the distance at which the potential reaches its minimum. At r_m , the potential function has the value $-\epsilon$ that means the distances are related as $r_m = 2^{1/6}\sigma$. However, since the L-J potential only calculates the distance between pair atoms but ignores the effect of the atomic structure, it is not adapted to simulation the FCC to BCC phase transformation in this research.



A figure shown the L-J potential profile. The potential energy $V(r)$ is the sum of the attractive function $-B/r^6$ and the repulsive function $+A/r^{12}$. The potential well depth ϵ is the minimum potential energy an atom can have, when it locate at its equilibrium position.

The embedded atom model (EAM) is another approximation describing the energy between two atoms. The original model was first developed by Murray Daw and Mike Baskes [7, 8] in 1983. In the basic model, the energy is a function of a sum of functions of the separation between an atom and its neighbors. The starting point of the EAM is the observation that the total-electron density in a metal is reasonably approximated by the linear superposition of contributions from the individual atoms. The electron density in the vicinity of each atom can then be expressed as a sum of the density contributed by the atom in position plus the electron density from all the surrounding atoms.

Finnis-Sinclair [10] is a specific type of EAM model for metals. Based on the normal EAM framework, the energy of an assembly of N atoms is given by

$$E = \frac{1}{2} \sum_{i \neq j=1}^N V_{ij}(R_{ij}) - \sum_{i=j}^N F(\rho_j) \quad (10)$$

with

$$\rho_i = \sum_j \Phi(R_{ij}) \quad (11)$$

In this expression, the total potential energy in the EAM is divided into two contributions, namely a pairwise part and a local density part. In these equations, the subscripts i and j label distinct atoms, N is the number of atoms in the system, R_{ij} is the separation between atoms i and j , ρ_i is the electron density at atom i due to the remaining atoms of the system, $\Phi(R_{ij})$ is the energy to embed atom i into the background electron density ρ and $V(\mathbf{R}_{ij})$ is the core-core pair repulsion between atoms i and j separated by the distance R_{ij} . F is an embedding function that represents the energy required to place atom i into the electron cloud. In Finnis-Sinclair, the embedding function is $F = -\sqrt{\rho_i}$. Therefore, by combining Eq.10 & 11, the Finnis-Sinclair EAM expression can be written as:

$$E = \frac{1}{2} \sum_{i \neq j=1}^N V_{ij}(R_{ij}) - \sum_{i=j}^N \left(\sum_{j=1}^N \Phi_{ij}(R_{ij}) \right)^{1/2} \quad (12)$$

A cutoff radius R_c has been chosen to limit the number of atomic interactions. When R_{ij} is greater than R_c , the value of V has already become very small and the potential is set to zero at this distance. The cut off radius has been chosen as $R_c = R_{2e} + \frac{R_{3e} - R_{2e}}{2}$ with R_{2e} and R_{3e} as the second and third neighbor distances. Comparing with the L-J potential, EAM-fs is a many-body potential. EAM-fs not only calculates the pairwise effect of atoms but also considers the structure and electron cloud contribution for the atomic system. Therefore, EAM-fs is more proper to simulate the FCC-BCC transformation than L-J formalism. For More detail on the algorithm about EAM-fs can be found in references [7-11].

2.6 The choice of potential

Empirical potentials are commonly determined by fitting a proposed functional form to available data. These data may be obtained from either experimental measurements or first – principles calculations. Generally, the input data include such quantities for perfect crystals as lattice parameter, cohesive energy, elastic constants and unrelaxed vacancy formation energy. Based on previous researches, there are several extant potentials for iron like Johnson 1964[11], Pak and Doyama 1969[13], Osetsky et al. 1995[14], Ackland et al. 1997[15], and Mendeleev et al. 2003[12]. Unfortunately, no single form of these potentials can completely simulate all transformation and solidification situation of iron. For example, the Johnson 1964, Pak and Doyama 1969 and Osetsky et al. 1995 potentials are purely pairwise which means that they assume the elastic constants $C_{12} = C_{44}$ and the unrelaxed vacancy formation energy is equal to the cohesive energy [12]. However, most of the experiments show that the vacancy energy is about one third of cohesive energy.

Ackland et al. 1997 and Mendeleev et al. 2003 potentials are of the “pair-functional” form [16] based on the EAM and second-moment tight-binding model. The Ackland et al. 1997 potential was derived by fitting to the static properties of BCC Fe at zero temperature, whereas Mendeleev et al. 2003 potential also incorporates interatomic force information for the liquid derived from *ab initio* calculations. However, the FCC γ - iron is an unstable phase in all simulation temperature as will be discussed in Chapter 4. Figure 8 shows the comparison of Lennard-Jones potential with the Ackland et al. 1997 and Mendeleev et al. 2003 potentials.

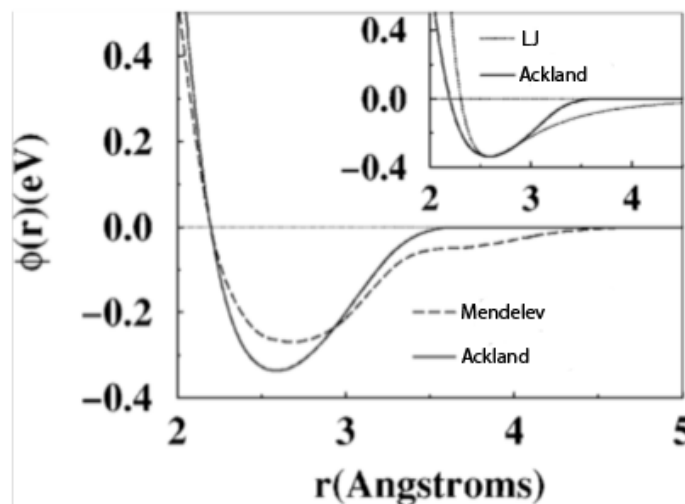


Figure 8 [17]

Effective-pair potentials derived from the Ackland et al. 1997 (solid line) and Mendeleev et al. 2003 (dashed line) many-body potentials for Fe. The inset compares the Ackland et al. 1997 pair potential (solid line) with a Lennard-Jones (LJ) potential (dashed) having the same well depth and equilibrium interatomic separation. (D.Y. Sun et al. 2004[17])

In the inset figure, the Lennard-Jones potential chooses the same well depth and equilibrium atomic spacing as the Ackland et al. 1997 potential. It is obvious that the Ackland et al. 1997 potential is significantly shorter in range and less repulsive at short distances. It is the main reason why the Ackland et al. 1997 potential can obtain much better equilibrium FCC phase than the Mendeleev et al. 2003 potential.

Therefore, the Ackland et al. 1997 potential is selected as the EAM-fs potential to process the movement of the α - γ interphase. However, since the EAM-fs formalism still does not account properly for magnetic effect, the Ackland et al. 1997 potential will probably not reproduce the iron phase diagram quantitatively. Based on the Ackland et al. 1997 potential, the free energy of the BCC phase is always lower than the FCC phase in the whole temperature profile (shown in Chapter 4), which is not matching the experiment profile. However, it is not the real problem. As long as the free energy difference for these two phases is predicted reasonably well in the simulated temperature range, this EAM-fs potential is very likely to be useful in the interphase mobility. More information about the algorithm and results of the Ackland et al. 1997 potential can be found in Appendix B.

Chapter 3

Previous work

This chapter will review some previous works on the kinetics of the α/γ phase transformation. These works will be discussed in term of the experimental research (3.1) and simulation area (3.2) separately.

3.1 Experimental research

The α/γ phase transformation was discovered hundreds of years ago and ever since then many experiments, theories and models have been done in this area. However, most of these experiments focused on the martensite formation of the Fe alloy, which limited the experiments to be conducted at low temperature (<1000 K) and could not use pure iron as the experimental element. In an early publication of the mobility of α/γ interfaces, Hillert [21] was forced to base his discussion on the assumption that the mobility is essentially the same for α/α grain boundaries and α/γ phase interfaces in an isothermal transformation. It was estimated as:

$$M = 0.035\exp(-147000/RT) \text{ m}^4/\text{J-s} \quad (13)$$

However, most of the latter studies showed that the mobility of the interface in the $\alpha \rightarrow \gamma$ transformation was several orders of magnitude below the values stated in Eq.13. For example, Krielaart and Van Der Zwaag [22] measured the rate of the massive transformation in a Fe-Mn alloy without C and evaluated the mobility of the interface to be:

$$M = 0.058\exp(-140000/RT) \text{ m}^* \text{ mol}/\text{J-s} \quad (14)$$

Using the molar volume $V_m = 7 \times 10^{-6} \text{ m}^3/\text{mol}$. found by Hillert [21], Eq.14 can be written as:

$$M = 4 \times 10^{-7} \exp(-140000/RT) \text{ m}^4 / \text{J-s} \quad (15)$$

This value was then applied successfully to describe the growth rate in the Fe-C alloys. Another new result reported by Wits et al. [23] gave somewhat higher values. They used Fe-X alloys, where X represents successively about 1 or 2 at.% of Co, Cu, Mn, Cr or Al, and proposed the following expression:

$$\begin{aligned} M &= 2.4 \exp(-140000/RT) \text{ m}^* \text{ mol} / \text{J-s} \\ &= 1.7 \times 10^{-5} \exp(-140000/RT) \text{ m}^4 / \text{J-s} \end{aligned} \quad (16)$$

Furthermore, Vooija et al. [24] presented even higher values in the Fe-Co and Fe-Cu alloy, which were still far below the proposed expression for α/α grain boundary given in Eq.13. Figure 9 shows the collection of these Fe-alloy experimental results by Hillert and Höglund [1].

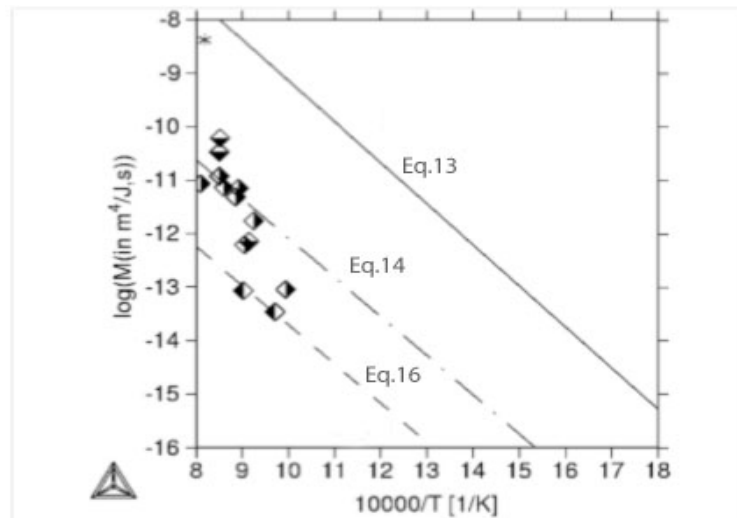


Fig. 1. Previous data on the mobility of α/γ interfaces obtained from the massive transformation. (*): Speich et al.[25], (◆): Krielaart et al. [22], (◈): Wits et al.[23], (◉): Vooijs et al.[24].

Figure 9 [1]

In Figure 9, Eq.13, 14 and 16 are indentified in the form of $\text{Log}(M)$ versus $10000/T$. Although the discrepancy is large, most of the data still lie between the lines of Eq.14 and 16, which is far below the proposed expression for α/α grain boundaries given in Eq.13. Only the data from Speich et al. [25] is somewhat closer to the values in Eq.13. However, the $M_{\alpha/\alpha}=M_{\alpha/\gamma}$ assumption and Eq.13 [1] are derived from Speich's results. Therefore, such data cannot be considered as a reference point. Moreover, due to the technical difficulties to use pure iron as experimental element and industrial interest, all of these results are based on the Fe-alloy. Even though the experiments are under the massive transformation condition, the diffusionless impurities still act as solute drag to slow down the interface velocity and reduce the mobility.

In order to further judge Hillert's assumption, more accurate data are needed. Figure 10 compares the new evaluation of the mobility of the α/γ interface in high pure Fe (99.98wt.%) cases collected by Liu et al. [26], [27] together with the data from Jones et al [28]. An interesting result from Jones and Pumphrey [28] shows that the mobility is not much different for the $\alpha \rightarrow \gamma$ and $\gamma \rightarrow \alpha$ transformation. The general impression from their information is that the temperature dependence is very weak. However, it should be emphasized that the massive transformation character becomes more obviously towards lower temperature. Therefore, one data point of the low temperature range ($10000/T = 17.4$) is very close to the line depicted by Eq.13 in Figure 10. However, because of the effect in low temperature, more detail research needs to focus in this area before making the conclusion. In addition, most of the data points are around the line described by Eq.16. Thus, Hillert and Höglund [1] concluded in their publication that the actual mobility values were much lower than that given by Eq.13.

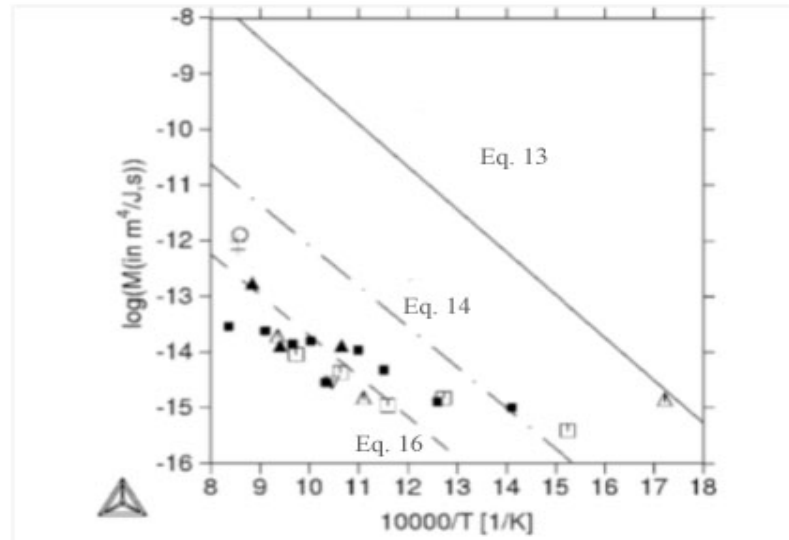


Fig. 3. New data on the mobility of α/γ interfaces obtained from the massive transformation. (+): $\gamma \rightarrow \alpha$ in Fe, Liu et al.[26], (O): $\gamma \rightarrow \alpha$ in Fe-Co and (∇): $\gamma \rightarrow \alpha$ in Fe-Mn, Liu et al.[27], (■): $\alpha \rightarrow \gamma$ in Fe-Ni, (□): $\gamma \rightarrow \alpha$ in Fe-Ni, (▲): $\alpha \rightarrow \gamma$ in Fe-Mn and (Δ): $\gamma \rightarrow \alpha$ in Fe-Mn [28].

Figure 10[1]

Furthermore, Hillert and Höglund [1] also tried to use the current information to build up a model for fitting the experimental data. According to their assumption, The total chemical driving force for the diffusionless $\gamma - \alpha$ transformation is assumed to start from zero at some temperature, T_{start} , below the equal Gibbs energy temperature T_0 , as shown in Eq.17.

$$\Delta G_m = G_m^\gamma(T) - G_m^\alpha(T) - G_m^\gamma(T_{start}) + G_m^\alpha(T_{start}) \quad (17)$$

All α nuclei are assumed to start growing spherically at T_{start} and combining with Eq.1 we obtain

$$R = \int_{t_{start}}^t v dt = \int_{T_{start}}^T v dT / C = (M / CV_m) \int_{T_{start}}^T \Delta G_m(T) dT \quad (18)$$

If the mobility M and the cooling rate C are considered as constant and using Kolmogorov's analysis [48] of impingement, the α phase fraction can be expressed as:

$$\ln(1-f) = \ln\left(\prod_i (1 - R_i^3/R_0^3 N)\right) = \sum_i \ln(1 - R_i^3/R_0^3 N) \cong -\sum_i R_i^3/R_0^3 N = -R^3/R_0^3 \quad (19)$$

In which, N is the number of α grains in the whole system and R_0 is the average size of the final α grains. Inserting R from Eq.18 as R_i calculates the fraction transformation. Hillert and Höglund tried to validate this model by comparing their results with one of the experimental curves published by Liu et al. [26]. As shown in Figure 11, it evidenced that the complete curve is not reproduced very well.

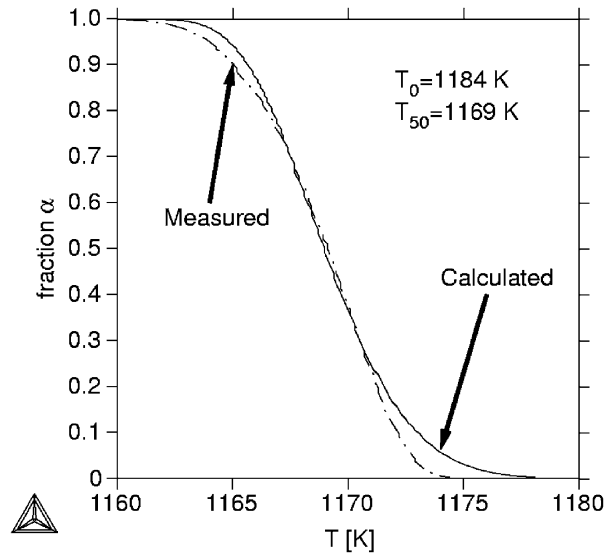


Figure 11. [1]

Transformation curve for $\gamma \rightarrow \alpha$ in Fe. The measured values was obtained using a continue cooling method, and the calculated curve was base on the parameter values $T_{\text{start}}=1184.5\text{K}$ and $M=1.0 \times 10^{-12} \text{m}^4/\text{J-s}$

This simple model shows an obviously unrealistic result at low and high degrees of transformation. One of the reasons that caused these deviations could be the mobility and the interface velocity parameter. Since these parameters are hard to be detected in the experiment, more studies are needed to focus on these areas to improve the model.

The above discussion illustrates that there is still deficiency in previous experiments. First of all, most of the up-to-date experiments still focus on Fe alloys. This gives uncertainty when determining if the specimen did transform by a purely massive mode, and how much does the impurity drag affect the interface. That is why Hillert and Höglund also suggested in their review paper that, “The effect of the interstitial content should be studied and one should in general use the lowest possible impurity contents”. [1] Secondly, all of the previous results were obtained by the continuous cooling method. That means the interface is not moving in an equilibrium state. However, all of the assumption and model were built under an equilibrium state. As a result, more studies are still required in order to understand the effect of this continuous cooling and the cooling rate.

In summary, based on these experimental results, the activation energy was identified to be around 140 kJ/mole and the mobility was $10^{-6} \sim 10^{-9} \text{ m}^2 \cdot \text{mol}^{-1} \cdot \text{s}^{-1}$. However, the model still does not fit to the measurement very well. The impurity and the unequilibrium state are the main reasons that lead to the variance. In this thesis, we assume that the massive transformation for pure iron can be considered as the initial state of the Fe $\gamma \rightarrow \alpha$ transformation. At that moment, all the driving force is applied to activate the transformation and the transformation is purely interface control. In addition, the results for pure iron can be used to build the basic model for the transformation. The effect of the impurity can be represented as parameters and added to the model for the pure iron case. Therefore, finding the mobility and activation energy in pure iron is the foundation to build a universal model for the Fe $\gamma \rightarrow \alpha$ transformation. It is also the main objective of this research.

3.2 Simulation area

With the continuous development and improvement of computational technology, use of the computers to simulate and study the massive transformation process becomes possible. The advantage of using simulation technology is that simulation can avoid the effect of the experimental environment like impurities in the sample and can maintain an isothermal conditional. Thus, this method can simulate the massive transformation in an ideal situation.

The most recent simulation investigation of the α/γ phase transformation was performed by Bos, Sietsma and Thijsse [33]. In their simulation, Bos et al. used the MD method and the Johnson-Oh EAM potential for Fe to successfully build up a system to simulate the martensite transformation in pure iron case. In Bos's simulation system, full periodic boundary conditions were not used. As shown in Figure 12, in order to let the atomic structure to be sheared, at least one pair of the boundaries which are perpendicular to the α/γ interface have to be free surface. They tested the boundary setting in two different interface orientations which are A. $\{100\}_{fcc} // \{110\}_{bcc}$, $\langle 100 \rangle_{fcc} // \langle 011 \rangle_{bcc}$ and B. $\{111\}_{fcc} // \{110\}_{bcc}$, $\langle 112 \rangle_{fcc} // \langle 011 \rangle_{bcc}$. Both of these boundaries setting had the flat interface surfaces. They didn't observe any α/γ phase transformation phenomenon in full periodic boundary condition.

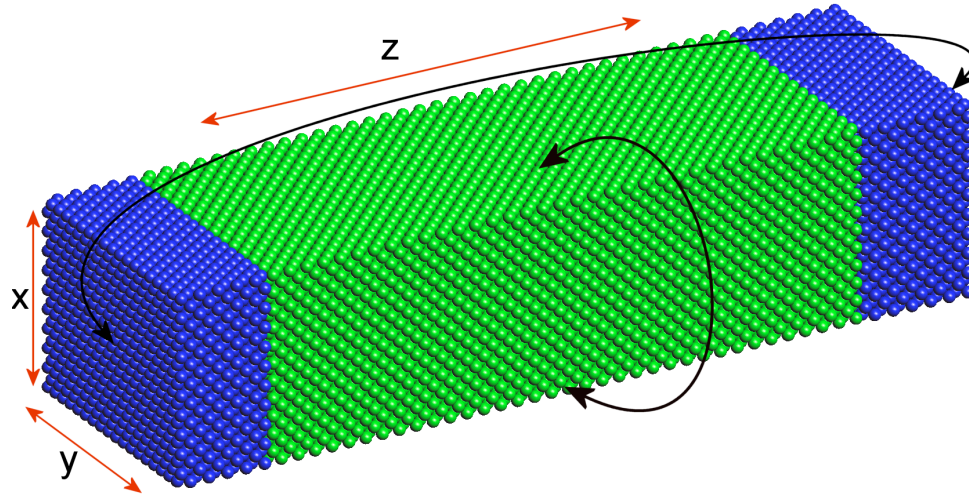


Figure 12 [33]

A typical simulation box used in C.Bos et al. research. The x direction in the figure coincides with the fcc [110] direction, y with fcc [010], and z with fcc [001]. The two yz-boundary are non-periodic (free surface).

In addition, Bos et al. observed an incubation time before the transformation started. They consider that the incubation time is caused by the rearrangement of the interface atoms, since the BCC and FCC have 0.2% lattice parameter difference. Therefore, the time period, which is required to let the interface deform and release the interatomic stress, is the incubation time. For the same reason, in the full periodic boundary condition, there is no free surface to allow the flat interface to distort and release the misfit interatomic stress. Thus, no interface mobile is observed in a flat FCC – BCC interface setting under the full periodic boundary condition. In addition, Bos defined that the transformation speed relates to the temperature and the volume to surface area ratio (V/A). However, because the free surface is used in the simulation box, the activation energy is actually reduced. Therefore, Bos et al detected a high interface velocity and mobility up to 400 m/s and 0.3 m³/mol/J-s. According to their results, the activation energy is only around 5.8 kJ/mole. Since the objective of Bos's research was to simulate the martensite transformation, their results are still inapplicable in the massive transformation model. In our research, we try to use the full periodic boundary to simulate the massive transformation and the results will be compared to both of the experiment and simulation data in Chapter 5.

Chapter 4

Approach

The approach for computing the mobility of the massive transformation is based on the time dependence of the changing potential energy. As shown in Eq.4, the interface velocity can be calculated by the first derivative of the potential energy. On the other hand, the driving force controls the interface speed and determines the mobility according to Eq.2. Therefore, the simulation box setting must have the possibility to obtain these potential energy and driving force information. First of all, the melting point (4.1), which based on the Ackland et al. [15] iron potential has to be identified. Then, a reasonable temperature range can be chosen to do the simulation. The melting temperature also will be useful in calculating the driving force. Second, the free energy function can be built up by comparing the potential energy difference between the solid and liquid phases. The free energy difference between the FCC and BCC phases is the driving force (4.2) of the transformation, which can be identified at a given temperature. Meanwhile, the lattice parameters for FCC and BCC can be measured at the same time and this information will be used in the interface set up. Third, in order to resemble the reality, we try to establish full periodic boundary conditions to simulate the transformation. Therefore, the interface orientation (4.3.1) and the dimensions of the simulation box for each phase (4.3.2) have to be selected carefully to avoid an external stress, which can affect the result. Finally, the system has to be equilibrated (4.3.3) before acquiring the data.

4.1 Melting temperature

In MD simulation, the melting temperature of the material depends on the EAM potential that is chosen. Measuring the melting temperature is always the first step to prepare for a MD simulation. Since the free energy of the solid and liquid phases is equal to the melting temperature (T_m), an accurate determination of T_m provides a convenient reference point from which the free energies versus temperatures can be specified. In this research, we use the Ackland et al. 1997 [15] iron potential. Since the austenite – ferrite transformation occurs in the low temperature range, the simulation temperature range has to be far away from the melting point. On the one hand, low temperature can reduce the effect of the high kinetic energy of the atoms and approach the real massive transformation temperature range. On the other hand, simulating in the low temperature range can also avoid the grain boundary premelting [34] to happen on the α/γ interface to effect the transformation.

In this thesis, a coexistence simulation method, which has been developed by Morris and Song [35] is used to identify the melting point. In their method the solid and liquid phases are equilibrated in one coexistent system to determine the melting temperature. The basic algorithm is to use equilibrium free energy calculation [35], which means calculating the zero Gibbs free energy temperature of both phases, the melting temperature is determined directly using the relationship

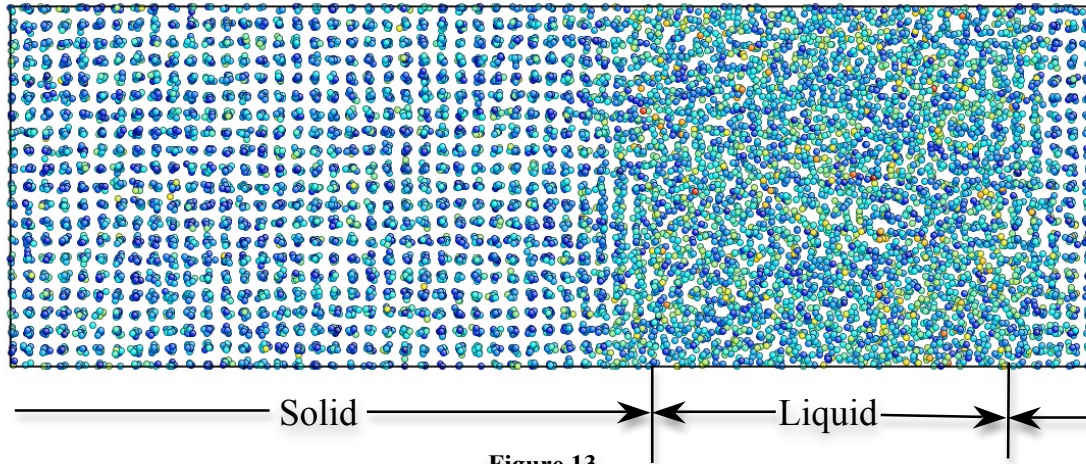
$$g_s(P, T_m) = g_l(P, T_m), \quad (20)$$

where $g(P, T)$ is the Gibbs free energy per atoms, the subscripts s and l indicate the solid and liquid phases, and $T_m(P)$ is the melting temperature at a given pressure. Typically, the system evolves in a microcanonical ensemble (NP_xH) system, which means constant pressure, number of atoms and enthalpy. In this case, if the system's temperature is initially higher than the melting temperature, then some of the solid phase will melt. This requires latent heat, and therefore converts some of the kinetic energy to potential energy

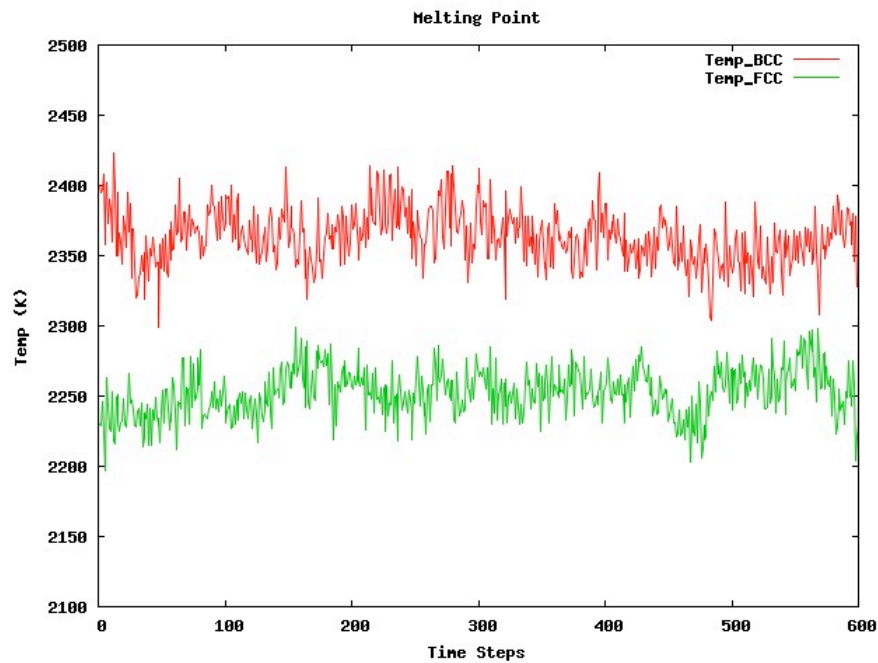
and reducing the temperature. In this way, the system is stable at its melting temperature from above. Using the same idea, if the initial temperature is too low, it will approach to the melting temperature from below.

In our temperature range, iron has two solid phases: α -BCC and γ -FCC. They have different melting temperatures. Therefore, we have to calculate their melting temperatures separately. To start the simulation, two simulation boxes with the identical dimension 30 by 10 by 10 unit cells are set up separately with α and γ phase pure iron. Then the two boxes are performed near the estimated melting temperature individually, to achieve an approximately equilibrated initial condition. Next, a liquid region is created, by melting half of the original solid box with a temperature 50% above the estimated melting temperature. After that the liquid part is cooled down to the estimated melting temperature slowly. If the liquid part solidifies in a short MD time scale, we need to raise the estimated melting temperature. Otherwise, we use the full periodic boundary conditions and zero pressure Isothermal-Isobaric (NPT) ensemble to equilibrate the whole box (both the solid and liquid part) for 10000 MD time step. During this step, the interatomic force adjusts the distance between solid and liquid atoms and creates two solid-liquid interphases boundaries. Due to the zero pressure NPT ensemble, the pressure on the box boundaries will be reduced to zero by automatically adjusting the box dimensions. Finally, the system is allowed to equilibrate using an NP_xH ensemble. As the system is closed, the temperature and total energy will evolve. If the system achieves a coexistence condition, it naturally evolves to the equilibrium melting point. Otherwise, if the energy is too high (or too low), the system will melt (or solidify) to adjust its temperature and maintain the constant total energy by exchanging the potential and kinetic energy. During this melting temperature determination process, one has to avoid the condition where the whole system melts or solidifies which means the estimated melting temperature is too far away from the real situation, and has to be reset with a new estimated melting temperature to redo the simulation. Figure 13 is an example of the equilibrated FCC coexisting system with 12000 atoms. Figure 14 is the temperature

profile when the system is approaching equilibration for both FCC and BCC phases in NP_xH ensemble.



FCC coexisting system with 12000 atoms and full periodic condition. Two S-L interfaces exist in the box. The atoms are colored according to the centro-symmetric parameter.



NPH temperature profile to identify the melting point of FCC and BCC phase.

Base on this method, the melting temperature of FCC and BCC phases are 2236 K and 2358 K with the Ackland et al. 1997 [15] iron potential. Therefore, the simulation temperature range is selected from 600K – 1400K with 200K increments. These temperature ranges include 2 samples in low temperature cases (600K & 800K), 2 samples (1000K & 1200K) around the critical temperature for the γ - α transformation 1185K, and one sample in the high temperature case. All of these temperatures are at least 800K lower than the melting point.

4.2 Driving force and lattice parameter

The driving force and lattice parameter in each simulation temperature have to be determined, before we start to set up the simulation box. In the austenite – ferrite transformation the main driving force is the free energy difference between the FCC (austenite) and BCC (ferrite) phases. As shown in the Eq.1, identifying the initial lattice parameter and the free energy difference ΔG precisely is very important for the following steps. Therefore, two individual simulation boxes are set up with the size of $20 \times 20 \times 20$ unit cells. One is in the FCC structure and the other is in the BCC structure. Then, the two boxes are equilibrated separately in five different simulation temperatures. The boxes are first run under the NVT ensemble (constant the number of atoms, volume, and temperature) for two nanoseconds, followed by another six nanoseconds under NPT ensemble (constant the number of atoms, pressure, and temperature). Figure 15 is one of the examples to equilibrate the BCC phase at 1000K case. The BCC phase runs for a total time of eight nanoseconds. The fluctuation rate of the potential energy decreases and stabilizes in a certain range (-129827 eV \sim -129870 eV for 32000 atoms). After the system reaches the equilibrium state, lattice parameters and potential energy are recorded as shown in Table 1.

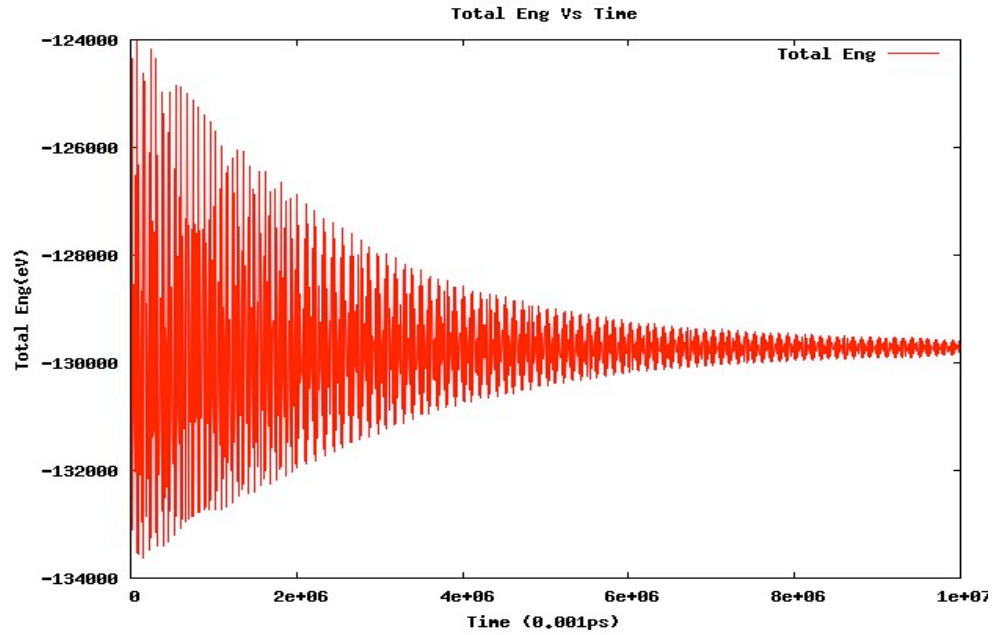


Figure 15

Potential energy graph for equilibrating BCC phase

Temperature (K)	Lattice Parameter (Å)	Potential Energy (eV/atom)	Lattice Parameter (Å)	Potential Energy (eV/atom)
	BCC		FCC	
600	2.8833	-4.2384	3.6842	-4.1844
800	2.8888	-4.2113	3.6874	-4.1590
1000	2.8946	-4.1821	3.6911	-4.1337
1200	2.9006	-4.1539	3.6953	-4.1073
1400	2.9070	-4.1235	3.6999	-4.0809

Table 1

Lattice parameter and potential energy for FCC and BCC phases in five different simulation temperatures.

Base on the Gibbs-Helmholtz Equations [36] (Eq.21), at the constant temperature condition, the free energy in the single phase system relates to its enthalpy difference at a specified temperature.

$$\left[\frac{\partial \left(\frac{G}{T} \right)}{\partial T} \right]_P = -\frac{H}{T^2} \quad (21)$$

Thus, Eq.21 can be integrated from the known melting point to obtain:

$$\frac{\Delta G}{T} = \int_T^{T_m} \frac{H^S(T) - H^L(T)}{T^2} dT \quad (22)$$

In Eq.22, ΔG is the free energy difference between the solid and liquid phases for either FCC or BCC. $H(T)$ is the enthalpy as a function of temperature T . The superscripts S and L refer to solid phase or liquid phase and T_m is the melting point. The numerator $H^S(T) - H^L(T)$ is the difference in enthalpy between the solid and liquid. To measure the latent heat, another two super cooling liquid simulation boxes are crated for BCC and FCC phases. These two boxes are set to pure BCC and FCC phases initially and melted at 3000K, and then they are slowly cooled down and equilibrated at the specified temperature. A comparison of the results is shown in Table 2.

Temperature (K)	Enthalpy (eV/atom)	Enthalpy (eV/atom)	Enthalpy (eV/atom)
	Liquid	Solid (BCC)	Solid (FCC)
1800	-3.8778	-4.0588	-4.0254
1900	-3.8531	-4.0420	-4.0107
2000	-3.8282	-4.0243	-3.9958
2100	-3.8028	-4.0066	-3.9804
2200	-3.7774	-4.3980	-3.9646

Table 2

Comparing result of the enthalpy for solid and liquid states for individual FCC and BCC phases. The temperature range is from 2200K to 1800K. Below 1800K the super cooling liquid phase is unstable.

From Table 2, in the super cooling range, the enthalpy for BCC is always lower than the FCC phase, and the enthalpy difference is very small. Based on above data, the linear enthalpy function can be identified as shown in Table 3. Based on the Eq.17, the FCC solid – liquid free energy function is calculated to be $G=7.540e^{-5}T-0.16907$ and the BCC function is $G=8.296e^{-5}T-0.19714$. Both of these values are in the unit of eV/atom. As shown in Figure 16, the red line identifies the FCC function and the blue is the BCC function. The distance between these two lines is their free energy difference, which is the driving force for the transformation.

	BCC			FCC	
T_M	2358 K		T_M	2236 K	
H(T)	L (eV/atom)	$H^L = 0.251T - 4.330$	H(T)	L (eV/atom)	$H^L = 0.251T - 4.330$
	S (eV/atom)	$H^S = 0.177T - 4.378$		S (eV/atom)	$H^S = 0.151T - 4.299$

Table 3

Melting temperature and the potential energy function for individual BCC and FCC phases.

In Figure 16, the two solid-liquid free energy functions are linear, which does not agree with the experiment value. In the experiment, because of the effect of the magnetic force in the iron atom, the FCC free energy function is a curve and the FCC phase can be stabilized at a certain temperature range. However, MD potential still cannot simulate the effect of the magnetic force even to this days, the EAM-fs potential will probably not reproduce the iron phase diagram quantitatively. This needs not to be a real problem. The objective of this research is to study the interface mobility in the FCC to BCC phase transformation; the central quantity is the free energy difference in the BCC stable temperature range. So if the free energy difference is predicted reasonably well for this temperature, this EAM-fs potential is very likely to be useful in the simulation of interface mobility. More improvement and future researches will be discussed in Chapter 7.

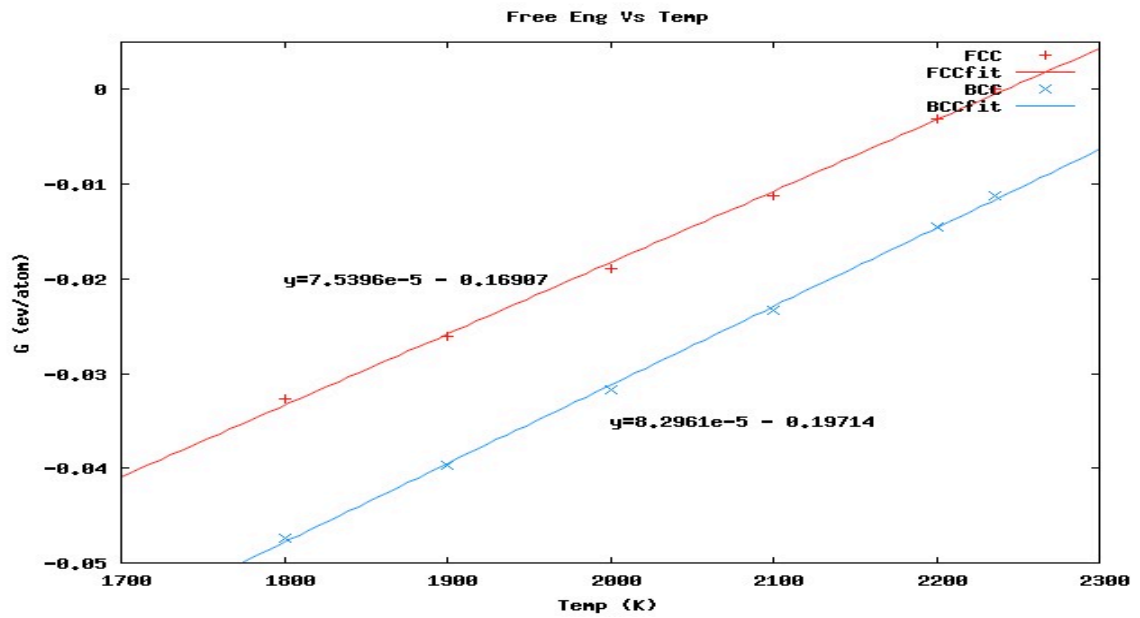


Figure 16

Free energy graph of temperature, which the red line is represent the FCC phase and the blue is the BCC phase. The distance between these two lines is the free energy difference between the FCC and BCC phases.

4.3 Simulation settings

After obtaining the necessary background information, we can start to choose the size of the simulation box and orientation. The interface set up, the boundary condition and the method of equilibration of the system will be discussed in detail in this section.

4.3.1 Interface

As discussed in Sections 2.5 and 2.6, the close packing interface Nishiyama-Wasserman (N-W) relationship with the disconnection step structure is used to connect the FCC and the BCC phase. Figure 17 is the side view of the interface setting and looking from the Z direction. Based on the N-W relationship we set the X direction as the growth direction that is perpendicular to the interface. That means the three coordinate directions for each phase are

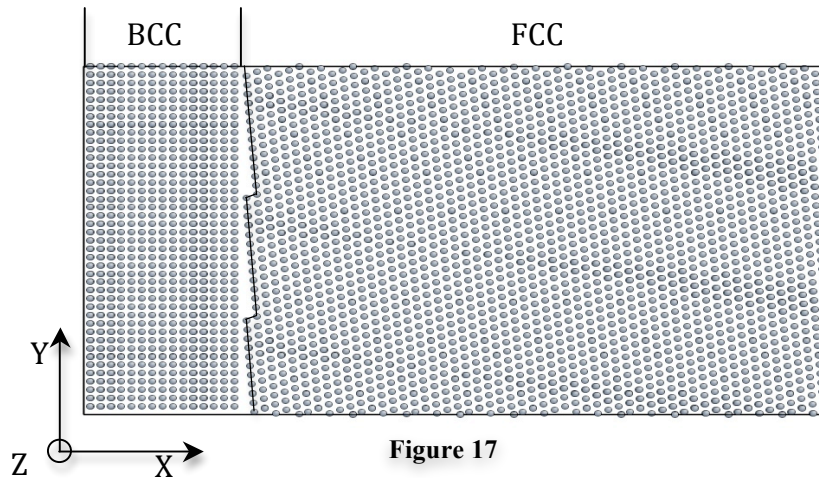
$$\text{BCC: } X [1 \ 1 \ 0], Y [-1 \ 1 \ 0], Z [0 \ 0 \ 1]$$

and

$$\text{FCC: } X [1 \ 1 \ 1], Y [1 \ 1 \ -2], Z [-1 \ 1 \ 0].$$

Furthermore, instead of rotate the FCC with X-axis in the real N-W relationship, we tilt the XY-plane of FCC box for 4.04° with the Z-axis fixed to create the step disconnection structure; In this strategy, three single atom height steps are created in the FCC interface and the three coordinate directions are transferred to be

$$X [7 \ 7 \ 6], Y [3 \ 3 \ -7] \text{ and } Z [-110].$$



2D view of the left end side of the simulation box. Looking downward in Z direction. FCC box is 4.04° tilted from the N-W relationship. Three single atom height steps structure are created in FCC interface with 14 layers of atoms in each steps.
 BCC: X [1 1 0], Y [-1 1 0], Z [0 0 1].
 FCC: X [7 7 6], Y [3 3 -7], Z [-1 1 0].

This disconnection structure is the key point to activate the transformation. First of all, the step structures increase the density of the matching atoms by creating perfect matching area in each ledge (Figure 5). In this way, inserting the monatomic ledge between coherent regions in the FCC/BCC boundary increases the frequency of repetition of these regions and raises the proportion of coherent atom in the boundary to around 25%. Second, the secondary disconnection forming in each terrace plane releases the plane stress created by the misfit dislocation [37], which will be discussed in Chapter 6. As shown in the Figure 17, \mathbf{b}_x is the vector of this plane strain in the terrace plane and \mathbf{b}_y is the vector defining the step strain, which is created by the disconnection. When the dislocation creeps to the edge of each step, the plane strain encounters with the step strain. Combining these two strains, now the net vector is perpendicular to the habit plane and the plane strain \mathbf{b}_x is no longer acting on the terrace plane. In this way, some of the plane stress is released by the disconnection structure. Third, the tilted FCC box with the periodic boundary condition transmits the disconnection through the transformation. We did not observed any γ - α

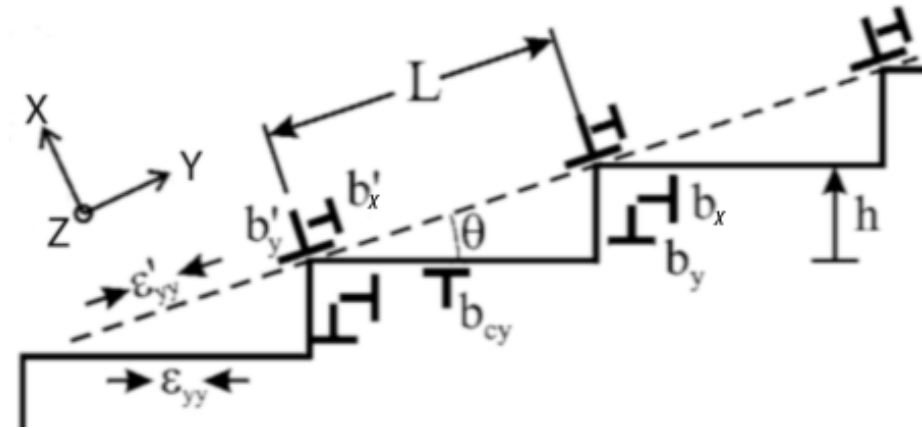


Figure 18 [37]

Schematic illustration showing the disconnection content of an interface, with Burgers vector components resolved in the terrace (upper) of the BCC phase and habit plane (lower) of the FCC phase. The terrace plane is inclined at an angle h to the horizontal habit plane. Coherency strain is represented by the equivalent “coherency” defect content b_x .

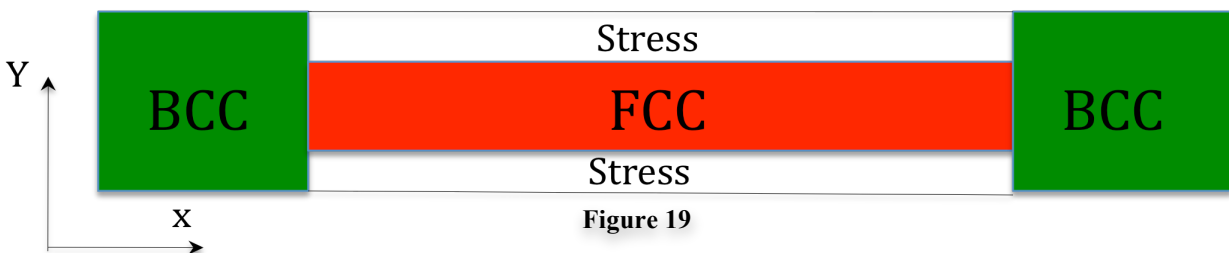
transformation in the planar interface with periodic boundary condition. However, using the step structure as shown in Figure 18 creates a low energy boundary to let the BCC phase nucleate and then activate the transformation. In addition, the step structure and the misfit stress form a secondary disconnection structure in each terrace planes to guide the growing of the BCC phase (discussed in Chapter 6).

4.3.2 System dimension

In this research, we use full periodic boundary condition for the box, which means the simulation geometry is periodic in all three dimensions and without any free surfaces. In this way, the model can simulate an infinite boundary situation and resembles more closely to the reality. Using the two Y-direction boundaries as an example, since the periodic condition once the atom moves past the top boundary under the periodic condition, it will appear back to the box from the bottom boundary and the atoms sitting on the top boundary will consider the atom on the bottom boundary as its neighbor (Figure 17). Thus, the dimension of the box needs to be selected carefully to avoid huge initial stress, which is created by the overlapping atoms, or too close to the boundary.

This is especially important for the FCC phase. Since the FCC box is tilted from its regular orientation, the atomic plane is no longer flat but contains steps in the X-direction. Besides, the atoms on the upper and lower Y directions periodic boundary have to fit in their lattice to evade the initial stress.

As shown in Figure 19, the whole simulation box is set up in a sandwich structure, in which the two sides of the box are BCC (ferrite) and the middle part is FCC (austenite). Since the lattice parameters for BCC and FCC are around 22% difference, the box size needs to be chosen carefully to make the interface fit to each other and avoid the stress during the phase transformation.



A sketch of the whole box setting. A miss match of the interface size can create a external stress, which can effect the final results.

Therefore, the interface size in the BCC phase is chose as 21 unit cells in the Y-direction and 27 unit cells in the Z-direction to match the FCC interface with 14.65 unit cells in the Y-direction, which is corresponds to 15 lattices in the untilted Y-direction and 15 unit cells in the Z-direction (Table 4). There are 180 layers of atomic planes in total in the X-direction, which are parallel to the interface, in the FCC phase. Based on our dimension setting, the difference of the interface lengths between FCC and BCC phases are less than 0.4% which will not cause an obviously effect in the initial pressure.

Phase	Size (NO. of unit cell)	Orientation	NO. of atoms
BCC	X (-4 4)	X [1 1 0]	18144
	Y (0 21)	Y [-1 1 0]	
	Z (0 27)	Z [0 0 1]	
FCC	X (-30.14 30.14)	X [7 7 6]	206190
	Y (0 14.65)	Y [3 3 -7]	
	Z (0 15)	Z [-1 1 0]	

Table 4

Dimension and orientation of BCC and FCC phase boxes and the number of atoms base on this setting

4.3.3 Equilibrate the system

Before starting the phase transformation simulation, the systems have to be equilibrated in their specified temperature to avoid the affect of the extra stress and the huge frustration of the potential energy. During the equilibration step, the atoms vibrate and adjust their positions to release their interatomic stress under isothermal-isobaric condition. With the temperature being constant, the atoms will vibrate and adjust their position until they reach the equilibrant state. In this research, since the free energy gradient is always exist between the FCC and BCC phases. The two phase boxes have to be equilibrated separately in the five experimental temperatures before joining them together. Based on the above setting, a FCC phase box and two identical BCC phase boxes are run in NVT ensemble for 2 nanoseconds to stabilize the atomic structure, and then equilibrate in NP_xT ensemble with 0 external pressure for another 6 nanoseconds. (Since the FCC box has much more atoms than the BCC box, it may require twice of the equilibrating time). NP_xT means fixing the Y and Z dimensions but only changes the box length in the X-box length. This ensemble can equilibrate the system without changing our initial interface dimension (Y-Z plane), which can avoid creating the misfit in the

interface when connecting the two phases. After the equilibration the whole box is connected as shown in Figure 20.

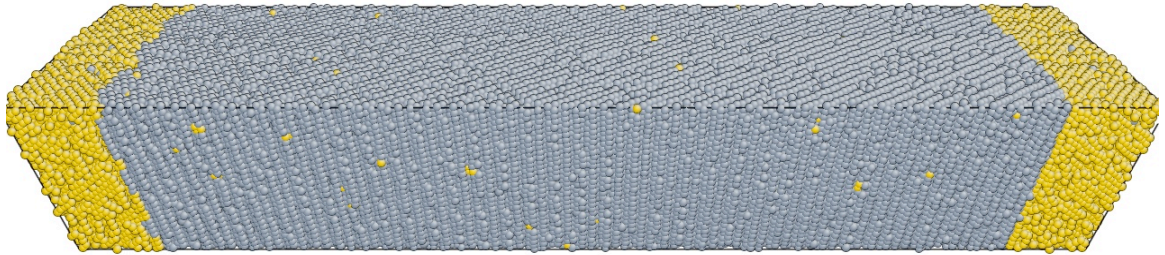


Figure 20

A schematic of the whole simulation box. Two BCC (golden atom) phase connecting two sides of the FCC (grey atom) phase to create two γ/α interfaces. The dimension of the box is $448.84\text{\AA} \times 85.6\text{\AA} \times 78.7\text{\AA}$ with total 241344 atoms.

Chapter 5

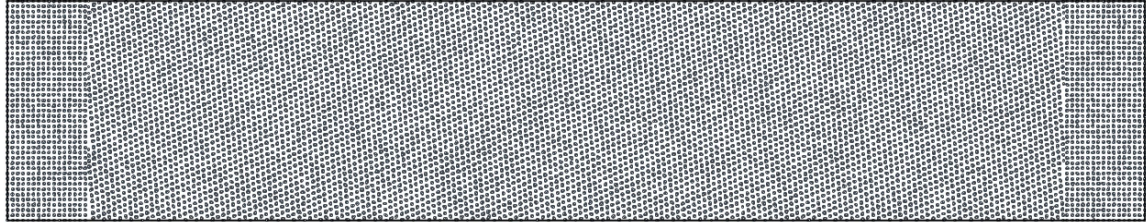
Results: interface velocity, mobility and activation energy

Based on the theory and the set up from the previous chapters, we can start to simulate the austenite to ferrite transformation and analyze the results. As discussed before, the potential energy profile (5.1) can be directly captured during the transformation. According to Eq.4, the interface velocity and mobility (5.2) can be calculated from the potential energy profile and simulation box dimension. Finally, the activation energy and the pre-exponential mobility factor (5.3) are obtained and will be compared with the experimental data.

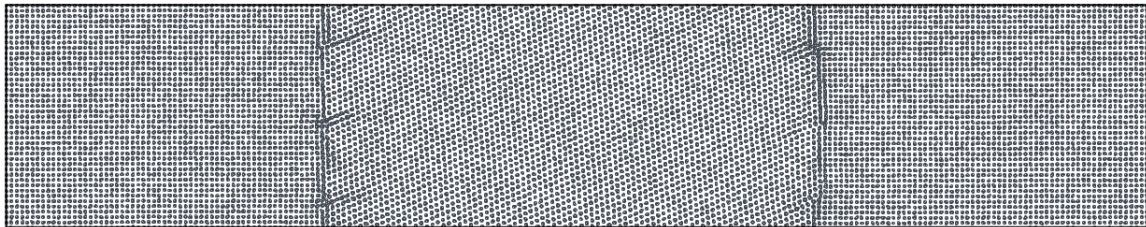
Based on the selecting temperature range (600K – 1400K), 5 samples are separated into 3 groups. These groups include 2 samples in low temperature range (600K & 800K), 2 samples (1000K & 1200K) around the critical temperature for the γ - α transformation (1185K), and one sample (1400) in the high temperature range. All of the five samples are established with identical box dimension, number of atoms (241344 atoms) and interface setting to do the compaction. Furthermore, all of the samples are equilibrated under their specified temperatures before starting the transformations.

After all the preparations, five samples are run in LAMMPS and repeated at least three times for each temperature. In each run, the initial ensemble of atom velocities [6] is changed to get average values. Figure 21 (a)-(d) is an example of the γ - α transformation process for the 800K case. Figure 21 (a) shows the initial state of the 800K simulation box. Two BCC phase boxes connect to the two sides of a long FCC phase box and there are three step structures on each interface. Figure 21 (b) is the snapshot after 5 nano-seconds of simulation runtime. The three step structures on the interface created three

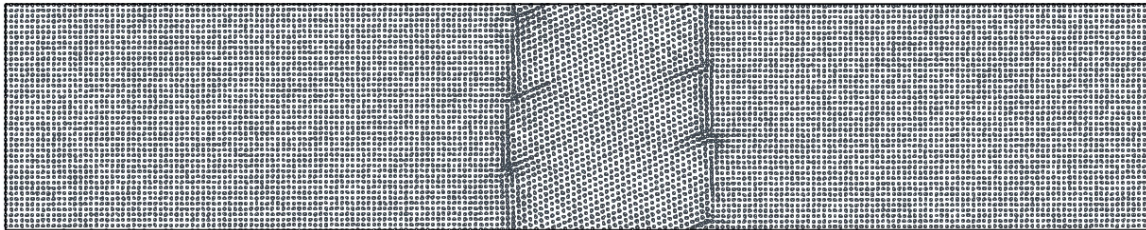
disconnection defects shooting into the FCC phase and glided following their Burgers vector direction during the transformation (More detail information about the interface mechanism will be discussed in Chapter 6). Figure 21 (c) shows the last state of the transformation, where concave structures are observed in both of the two interfaces when the two interfaces are very close to each other. The concave structures of the interface show a partial individual steps growing behavior and a slightly unbalance growing speed in each step, which make some of the steps grow faster than the others (more detail in Section 6.4). Figure 2. (d) shows the transformation already fully completed after 15ns. The whole simulation box is stabilized in pure BCC phase and without any defects.



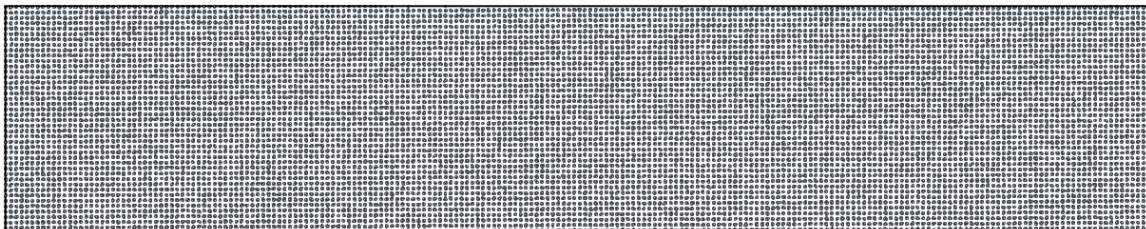
(a) 0 ns



(b) 5 ns



(c) 10 ns



(d) 15 ns

Figure 21

An example of the γ - α transformation process for the 800K case. (a) is the initial state of the simulation box showing a sandwich structure with 2 BCC phases connecting the two sides of a FCC phase. (b) and (c) shows the moving of the interfaces. (d) is the equilibrium BCC phase after the transformation.

5.1 Potential energy measurement

As shown in the free energy graph in Figure 16, since the BCC phase has the lowest energy state, the driving force will lead to a rearrangement of the FCC lattice to the BCC lattice. During the transformation, the total energy of the system will decrease. However, since both of the two phases are equilibrated at the simulation temperature before the transformation, the kinetic energy is already equilibrated to the steady state at that temperature. In addition, the NP_xT ensemble stabilizes the temperature of the system. Therefore, the variation of the total energy of the system is according to the change of the potential energy. The potential energy is one of the thermodynamic quantities, which can be directly obtained from the LAMMPS [6]. Thus, the potential energy versus time can be used to monitor the austenite to ferrite transformation.

5.1.1 Low temperature case (600K & 800K)

Figures 22 & 23 show the total potential energy versus time for the 600K and 800K cases. The total potential energy decreases as the interface moving. The potential energy fault at 16.8 nanosecond for 600K and 13.7 nanosecond for 800K is showing the moment at which the two interfaces contact each other. At this low temperature most of the iron alloys have undergone the martensitic transformation. However, since pure iron is simulated in these simulations, and we use the full periodic boundary condition, even in this low temperature regime the system still transform by a massive nature. For both potential energy graphs Figure 22 & 23, the level of decrease of the potential energy is fluctuating. At these temperature ranges, the low kinetic energy causes slowly moving of atoms. Sometimes, the interfaces have to slow down or even stop (for example the horizontal steps around the 5th nanosecond in Figure 22 and the 10th nanosecond in Figure 23) to let the interface atoms to gain energy and rearrange their positions. This long interface fluctuation time affects the final result significantly. For example in the 600K case, the shortest transformation time is 16ns but the longest transformation time requires

30ns. Thus, to minimize the fluctuation effect, only the 3 median values during the 5 runs for the same simulation boxes (only change the initial atoms' velocity) will be taken in the 600K case. The trend lines in both figures are fitted to the transforming part of the potential energy profile. The slopes of the trend lines identify the decreasing rate of the potential energy, which is also the $\frac{dE}{dt}$ term in Eq.4.

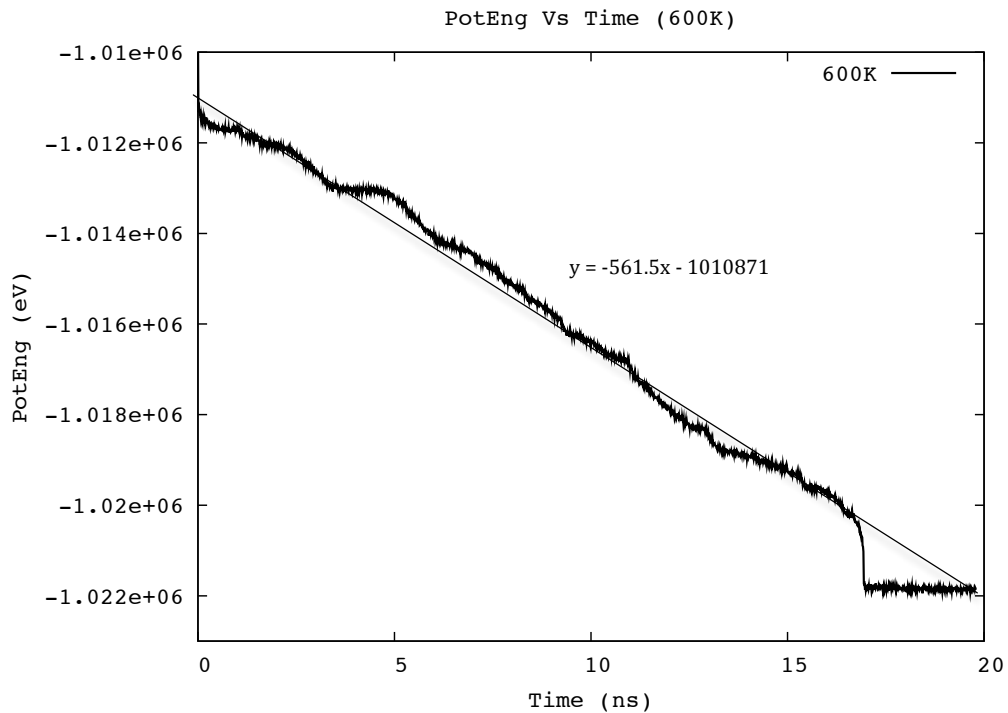
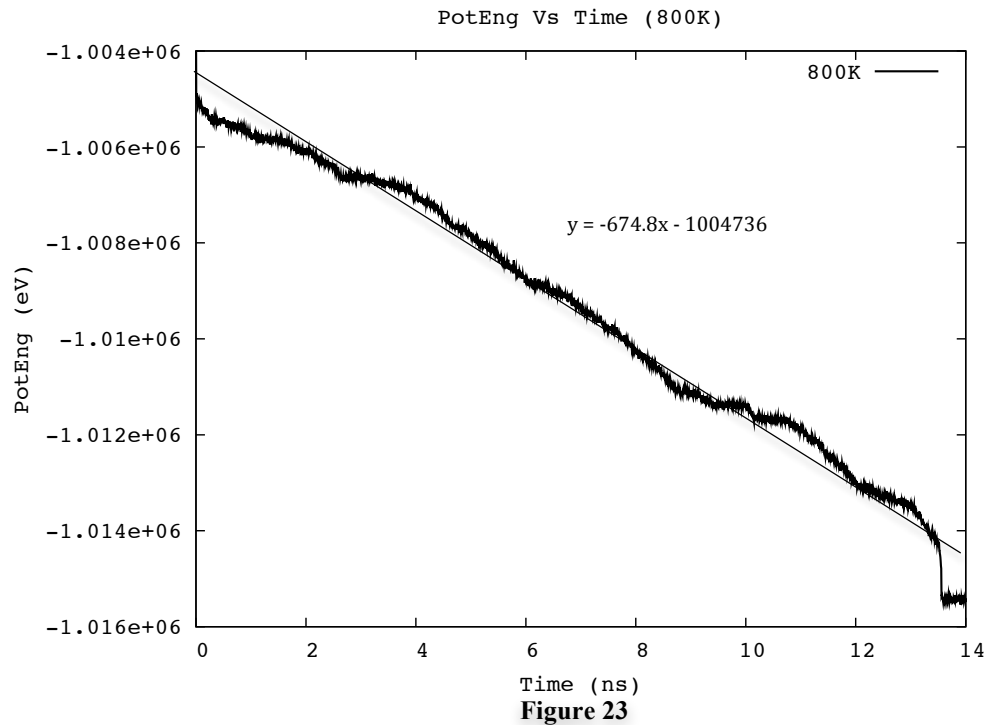


Figure 22

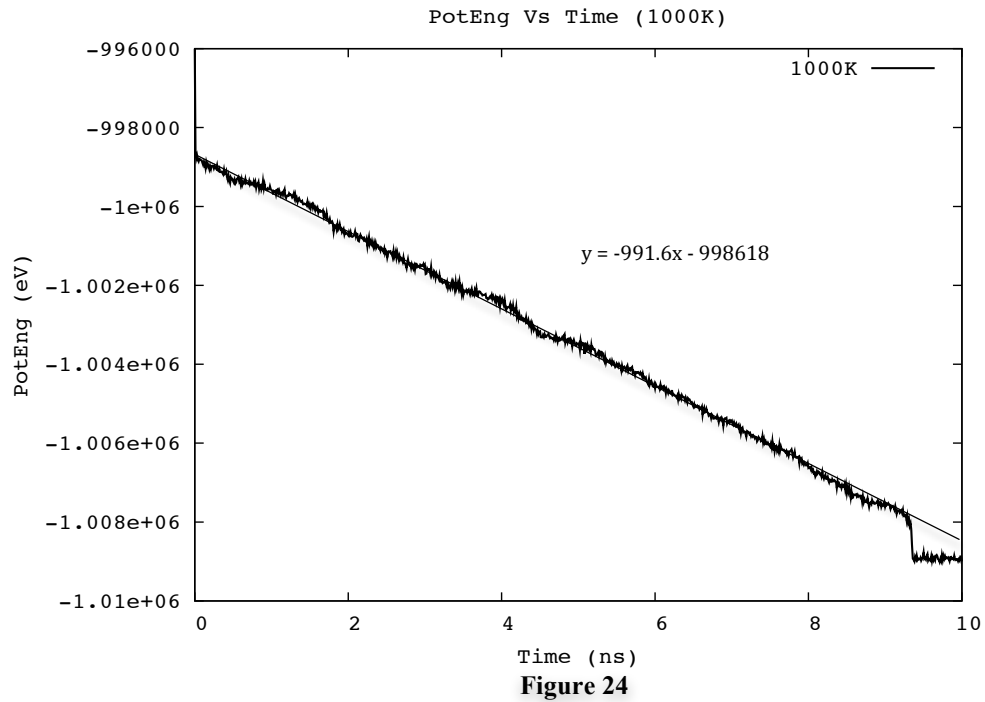
The potential energy Vs simulation time graph for 600K.
Trend line function: $y = -561.5x - 1010871$
 $dE/dt = -561.5$ eV/ns



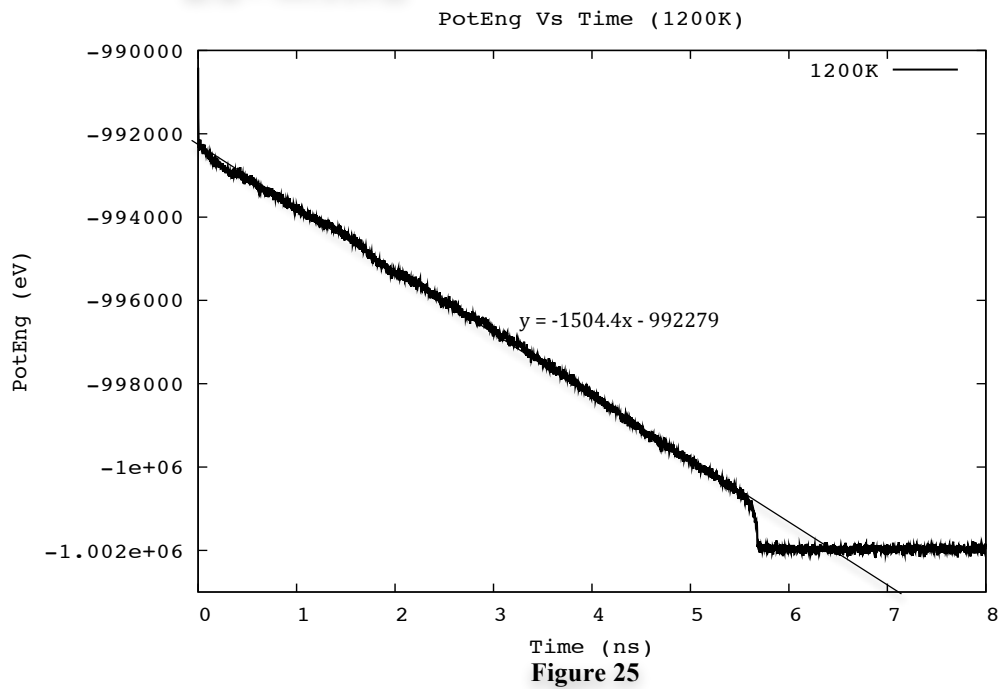
The potential energy Vs simulation time graph for 800K.
Trend line function: $y = -674.8x - 1004736$
 $dE/dt = -674.8 \text{ eV/ns}$

5.1.2. Normal transformation temperature 1000K and 1200 K.

From 1000K to 1200K is the normal temperature for the austenite – ferrite transformation. Compared with the low temperature cases, the transformation time is less in 1000K and 1200K cases. Further more, the potential energy versus time shown in Figures 24 & 25 are smoother than the low temperature cases (Figures 22 & 23). That means the high temperature increases the kinetic energy of the BCC iron atoms and speeds up the interface velocities. The high temperature also gives the iron atoms higher capability to cross the interphase boundary and reduces the fluctuation effect. Therefore, the interface velocities are more linear in this normal transformation temperature, which reflects on the profile as a smoother potential energy line and higher the energy decreasing rate.



The potential energy Vs simulation time graph for 1000K.
Trend line function: $y = -991.6x - 998618$
 $dE/dt = -991.6 \text{ eV/ns}$



The potential energy Vs simulation time graph for 1200K.
Trend line function: $y = -1504.4x - 992279$
 $dE/dt = -1504.4 \text{ eV/ns}$

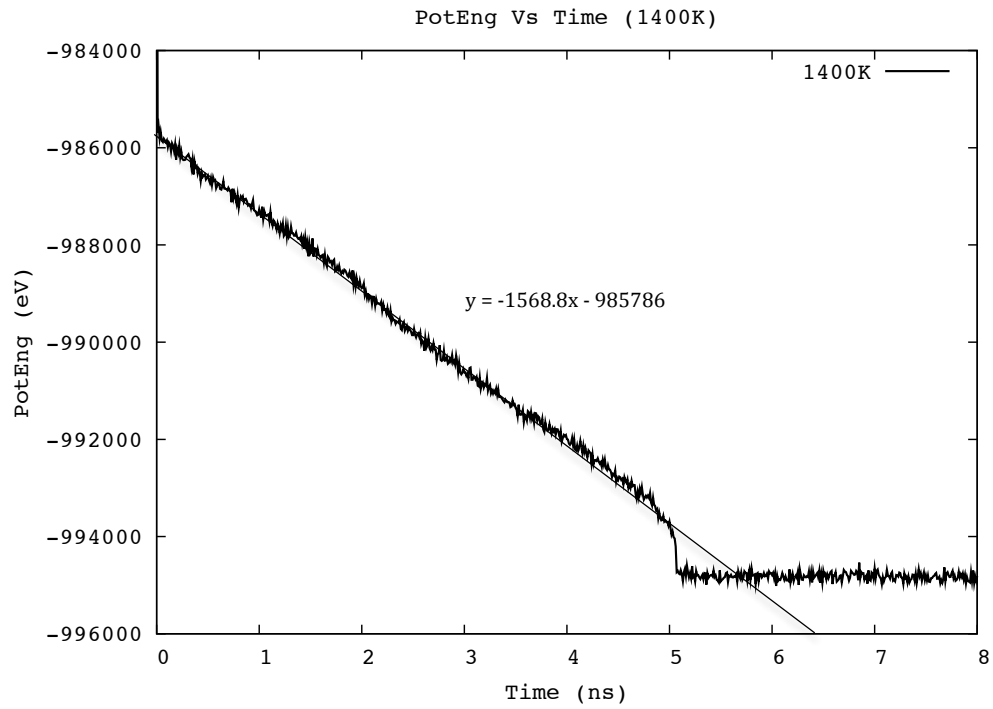
5.1.3 High temperature 1400K.

In most of the experiments, the austenite – ferrite transformation temperature is around 1184 K and the melting point of the δ BCC is 1809 K. However, since pure iron is used as the only element in this research, base on the Ackland et al. 1997 potential [15] the melting point of the δ BCC is up to 2358 K. And according to the free energy profile shown in Figure 16, the free energy line for BCC is always lower than that for the FCC in the whole solid range. Therefore, the transformation can also be simulated in the 1400 K temperature case.

Figure 26 is the potential energy Vs the simulation time graph for the 1400 K case. With the same dimension set up and has identical number of atoms as the 4 previous samples. The 1400 K case has the deepest decreasing slope and the smoothest potential energy profile, which means the fastest interface speed and therefore, as will be discussed in Section 6.3 it has the highest nucleation rate of BCC islands in the five samples. Since the driving force ΔG is almost constant during the transformation temperature range (Figure 16) while the kinetic energy is increasing with the temperature, based on Eq.1, the mobility can be written in form of

$$M = M_0 \exp\left(-\frac{E}{kT}\right) \quad (23)$$

in which the interface mobility is proportional to the temperature. Therefore, the mobility is under temperature control. It illustrates that the high kinetic energy let the atoms have greater capability to cross the interphase boundary. In addition, this high temperature transformation simulation also denotes that driving force ΔG identifies the probability of the nucleation in the interface and this driving force can be adjusted base on the EAM potential. Therefore, the velocity of the interface can be predicted in a reasonable temperature range, as long as we have precise driving force information.

**Figure 26**

The potential energy Vs simulation time graph for 1400K.
Trend line function: $y = -1504.4x - 992279$
 $dE/dt = -1504.4 \text{ eV/ns}$

5.2 Interface velocity, mobility and activation energy.

To calculate the velocity and the mobility of the interface during the transformation, we have to recall the dynamic function mentioned in Chapter 2 and combine our simulation box dimension with the driving force discussed in Chapter 3. A detailed calculation of 1000K cases will be analyzed as an example in here.

5.2.1 Interface velocity

Based on Eq.4, $v = -\frac{1}{2a\Omega L} \frac{dE}{dt}$ where the 2 in the denominator considers the two interfaces in the simulation box. a is the area of the interface. Since the y and z boundaries are fixed by the NP_xT ensemble, the interface area is equal to the y - z plane area, which can be calculated by the number of unit cell (Table 4) in the Y and Z direction times the lattice parameter (Table 1). The parameter L is the latent heat, which is the potential energy difference between the two phases (Table 1) and Ω is the volume per atom in the FCC phase, which is calculated by the volume of the unit cell (cubic of the lattice parameter Table 1) divided by the number of atom per cell (4 atom/cell for FCC phase). Finally, the first derivative of the potential energy $\frac{dE}{dt}$ is the slope of the potential energy profile shown in Figure 24 for the 1000 K case.

a – area of the interphase: 6737.0878 \AA^2

L – latent heat: -0.04842 eV/atom

Ω - volume per atom in the FCC phase: $12.5717 \text{ \AA}^3/\text{atom}$

$\frac{dE}{dt}$ - slope of the function potential energy profile: -991.6 eV/ns

Then,

$$v = -\frac{1}{2a\Omega L} \frac{dE}{dt} = \frac{1}{2 \times 6737.08(A^2) \times 12.57(A^3/atom) \times (-0.048eV/atom)} \times (-991.6eV/ns)$$

$$= 19.1 \text{ \AA/ns}$$

$$= 1.91 \text{ m/s}$$

5.2.2 Mobility

From Figure 16, the free energy function for FCC and BCC phases are indentified as:

$$G_{FCC} = 7.5396e^{-5}T - 0.16907 \quad (24)$$

and

$$G_{BCC} = 8.2961e^{-5}T - 0.19714 \quad (25)$$

Therefore, at 1000K the free energy difference $\Delta G = G_{FCC}(1000) - G_{BCC}(1000)$, which is equal to 0.0205 eV/atom.

In Eq.2, the $\vec{M}_0 \exp\left(-\frac{Q}{RT}\right)$ term can be considered as mobility M . Then Eq.2 can be converted to

$$M = -\frac{v}{\Delta G} = \frac{1.91m/s}{0.0205eV/atom} \times \frac{1}{1.0602 \times 10^{-19} eV/J} \times \frac{1}{6.0221 \times 10^{23} mol/atom}$$

$$= 9.657e-04 \text{ m*mole/J-s}$$

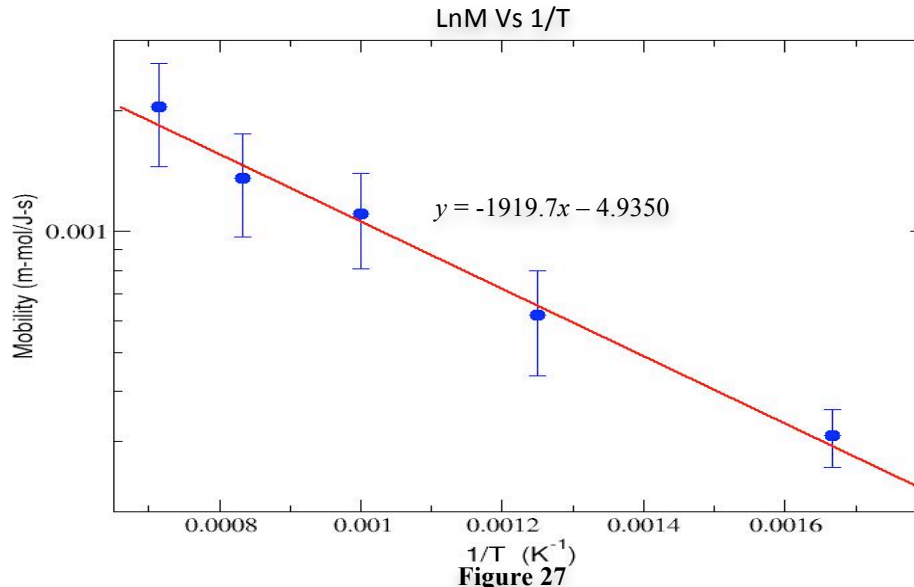
Table 5 shows the driving force, velocity, and the mobility in the five different temperature cases based on the calculation method list above.

Temperature (K)	600	800	1000	1200	1400
Driving Force (ΔG) (eV/atoms)	0.024	0.0220	0.0205	0.0190	0.0175
Velocity (m/s)	0.7 ± 0.201	1.3 ± 0.710	2 ± 1.028	3 ± 1.391	3 ± 1.720
Mobility (e-03) (m*mole/J-s)	0.31 ± 0.089	0.6 ± 0.334	1.0 ± 0.520	1.4 ± 0.759	$2. \pm 1.020$

Table 5
Driving force, velocity, and the mobility in the five different temperature cases

5.2.3 Activation energy and pre-exponential factor M_0

From the mobility data of the five different simulation temperatures, we can start estimate the activation energy. By taking the natural logarithm of the mobility term in Eq.1, a new linear function $\ln M = -\frac{Q}{R} \frac{1}{T} + \ln M_0$ is obtained. In summary all the five temperature cases, and the $\ln M$ Vs $1/T$ graph is shown in Figure 27. In Figure 27, the slope of the best fit line is the term $-\frac{Q}{R}$ (R is the gas constant), and the Y-intersect is the $\ln M_0$. Therefore, the activation energy Q and pre-exponential factor of mobility M_0 are calculated as 16 kJ/mole and 7.2×10^{-3} m*mol/J-s respectively.



The natural logarithm of the mobility versus one over temperature graph, with a best fit line function $f(x) = -1919.7x - 4.9350$;

5.3 Results and discussion

The transformation can be envisioned as the movement of atoms across the interphase boundary. Long – range diffusion does not occur in massive transformation. Therefore, the transformation rate can be described solely by means of the interface mobility. As introduced in Chapters 2 and 5, the interface mobility is defined as the proportionality factor between the interface velocity and the driving force for the transformation. In addition, in the isothermal condition the interface velocity of massive transformation will be constant throughout the transformation [4]. Then we can use a linear relationship trend to fit the transforming potential profile in Figures 22 – 26. Figure 28 shows a comparison of the potential energy during the transformation for five different temperature cases. All the samples have identical number of atoms, orientation and unit cell. However, because of the temperature variations, there are various in starting and equilibrium potential energy and transformation time.

The interface mobility and velocity model (Eq.2) uses three quantities to describe the phase transformation: the activation energy Q , the free energy difference ΔG and the pre-exponential factor M_0 . The activation energy Q is expected to be comparable to the value for nucleation rate of BCC crystal in pure iron [41]. Meanwhile, the nucleating energy relates to the composition, orientation and the driving force. In a certain orientation with single element condition, the transformation time decreases as the temperature raises, and when the driving force is constant. That is because based on the Ackland et al. 1997 iron potential, the change in driving force related to the temperature is very small. Comparing to the temperature effect to atomic kinetic energy, the temperature effect to our driving force is almost neglectable. Furthermore, in the identical composition, orientation and constant driving force situation, the higher temperature, the higher the total energy (both the potential and kinetic energy) of atoms, which means the atoms have more capability to across the interphase boundary. In this way, the high

temperature directly causes high interface mobility and hence reduces the transformation time. Thus, the interface mobility in our simulation is under temperature control.

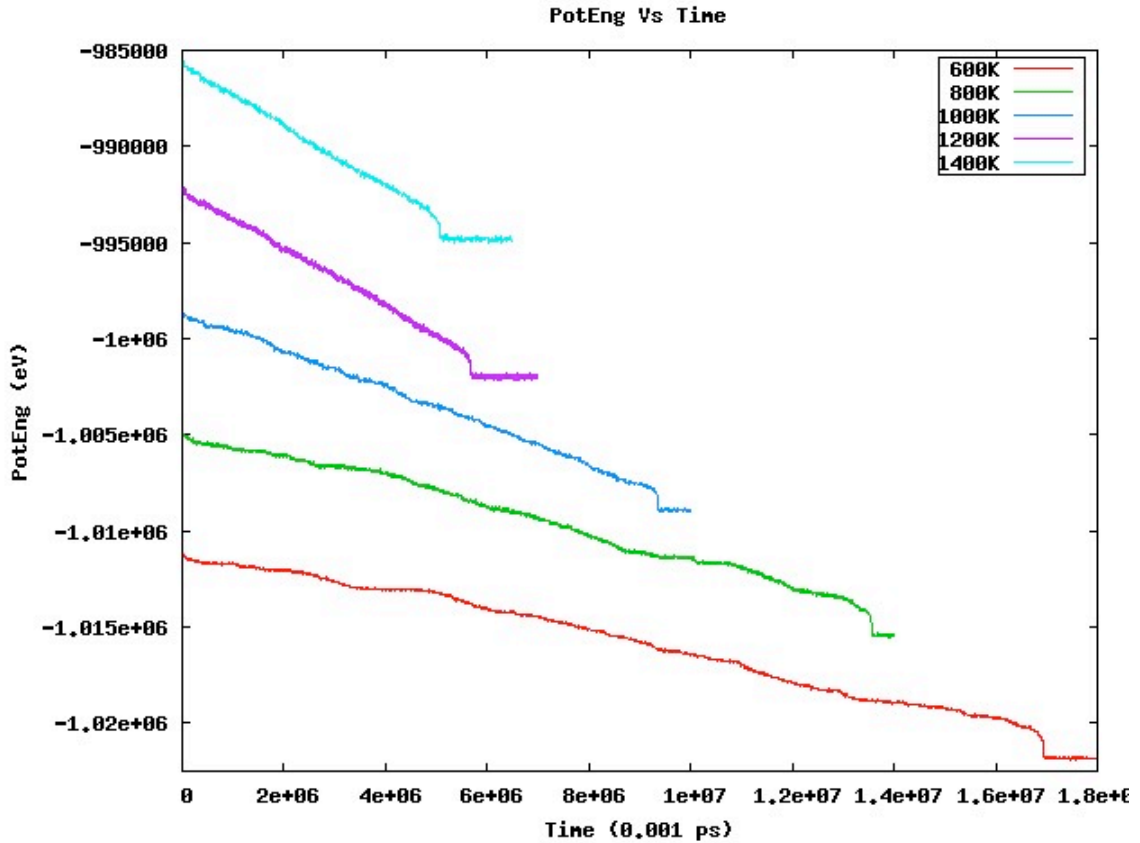


Figure 28

The potential energy profile during the γ - α transformation for five different simulation temperatures with the same setting of orientation, dimension and number of atoms.

The activation energy bases on our condition setting is 16 kJ/mole which is much smaller than the experimental value $Q = 140$ kJ/mole as shown in Table 6. However, some precious simulation studies shown that the activation energies values obtained from atomistic simulations are significantly smaller than those found in experiments (even in high purity materials) [9]. The difference comes from the affect of impurity and dislocations in the crystals. Most of the experimental values from researches are based on the iron alloy with adding the solute drag, which will increase the activation energy [51].

In simulation area, due to the low activation energy Bos's et al. detected a high interface velocity at 810 K to be around 400m/s (close to the martensitic transformation speed), and high mobility around 0.3 m*mol/J-s. However, our simulation box uses full periodic boundary without any free surface, so the activation energy (16 kJ/mole) is much higher than theirs, at 800K our mobility is 6.5×10^{-4} m*mol/J-s and the interface velocity is 1.4 m/s, which is more close to the massive transformations.

The most relevant experiment is approached by Liu et al [52]. During their experiment, 99.98 wt.% of pure iron is used as pattern to analyze the austenite-ferrite transformation behavior. Under an isochronal (continuous cooling) condition, Liu et al determined the average interface migration velocity is around 3×10^{-6} m/s and $Q = 147$ kJ/mole. However, that unknown 0.02 wt.% impurity can affect the interface velocity significantly. Rutter and Aust's [53] measure the grain boundary migration rate in Pb bicrystals as a function Sn content in one of their study. They demonstrate that even a 0.006 wt.% of impure Sn can slow down the grain boundary velocity by magnitude of 4. Therefore, more study should be focused on the influence of the impurity. Besides, the continuous cooling method induces a fluctuation of the net driving force, which leads to the irregular nature of the interface velocity, and affect the activation energy. Furthermore, Winning and Rollett declare that the dislocations in the grain impact the motion of the grain boundary [54]. During their experiment, the grain boundary is drove by the external stress in pure Al. Winning and Rollett found that the low and high angle grain boundaries show different behaviors when they cross the lattice dislocation. For the low angle boundaries sample, the grain boundary needs to climb over the dislocation by diffusing vacancies through the dislocation. It will take an extra activation enthalpy by 110 kJ/mole. For high angle grain boundaries, the dislocation can be absorbed by the grain boundaries and these processes require a lower activation enthalpy by 64 kJ/mole. In these simulation study, we have difficulty to identify the γ - α interphase boundary is belong to low or high angle. However, both of the cases required a much larger amount of energy compared with the energy activating the interface motion. Therefore, the impurity and dislocation are the main reasons cause the mismatch between experimental and simulation values.

Since in our simulation, the system is set in an ideal condition with 100 wt.% iron and none dislocation in the FCC phase. Indeed, the experimental activation energy is an average value for all grain boundaries [1]. However, some studies have shown that the transformation behavior is a strong function of the grain boundary orientation. In MD simulation, we can arbitrarily choose the grain boundary orientation. The interface relationship that is used in this study may be one of the low energy boundary relationships. Thus, a low activation energy is detected and directly contributes a high interface velocity and mobility. Therefore, the $Q = 16\text{kJ/mole}$ is consider as the primary activation energy to start the Austenite to Ferrite transformation and before the interface hit to and impure atoms or dislocations. Further studies relate to the influence of impurity, dislocation and interface orientations are processing.

Around 800K	Velocity (m/s)	Mobility (m*mol/J-s)	Activation energy (kJ/mol)
Massive transformation (Simulation)	1.4	6.2×10^{-4}	16
Martensitic transformation [33] (Simulation)	400	0.3	5.8
Diffuse control phase transformation [1] (Experiment)	10^{-3}	10^{-7}	140

Table 6

Compare the velocity, mobility and activation energy values from massive, martensitic and diffuse control phase transformation.

According to our study, using the MD method to study the γ - α massive transformation is feasible. Further study will focus on the following areas. First of all, new grain boundary orientations have to be tested to identify the effect of the orientations to the activation energy. Second, some impurity like carbon (C), manganese (Mn) or copper (Cu) can be added to study the possible effect of solute drag. Although the MD method cannot simulate the long-range diffusion process during the transformation, under the high interface speed situation, the solute drag can stay in their original position without diffusion with the interface. Some previous studies predicted that solute drags could act as a pin to slow down the movement of the interface. Therefore, clarifying the

property of the impure solute drags is helpful to explain the variance between simulation and experimental values. Third, dislocation can be created in the FCC phase to test the climbing or absorbing processing of the low and high angle boundary during the transformation. Finally, as discussed in Section 5.3, the driving force significantly affect the transformation behavior. The driving force in MD simulation is controllable by adding potential energy in specified lattice. For example, we can add the potential energy to the atoms belong to the FCC phase. In this way, we can adjust the driving force (Free energy difference between FCC and BCC phases) to match the experimental values and study the effect of the driving force to the transformation.

5.4 Summary

A molecular dynamic method to simulate the pure iron austenite – ferrite transformation has been demonstrated. Five different temperatures samples, from 600K to 1400K with 200 temperature increments are tested. The interface velocity and mobility are identified to be around 2m/s and $1e-03m^*mole/J-s$ based on the potential energy profile during the transformation. The activation energy is 16 kJ/mol, which is much lower than that found in previous experiments. The activation energy and interface velocity are related to the driving force, interface orientation and composition but also affect by the impurity and dislocation in the crystal. Based on the setting of our system and simulation method, further simulation research can be attempted to explain the character of driving force, interface orientation, lattice defect and composition during the massive transformation.

Chapter 6

Interface atomic mechanisms

With the MD method discussed in the previous chapters, the macroscopic data like the total potential energy, interface velocity and mobility are obtained. Now we can focus on some micro-phenomenon. The MD simulations can identify the coordinates of each atom and thus, track their motion during the transformation. In order to observe the moving interface, a centro-symmetry parameter is introduced in Section 6.1 to determine whether a given atom belongs to FCC or BCC phase. Based on previous studies, a step ledge growing behavior (6.2) is observed in some of interface orientations. However, according to our interphase boundary orientation, moving misfit dislocations also participate during the transformation (6.3).

6.1 Determine the interface

The α and γ grain boundary is a solid – solid interface. The difference of structures and the atom distances between the two phases are not as obvious as the solid – liquid interface. The common interface determining methods like the atom density or average atom distances are not precise enough to identify this solid – solid interface. Thus, a centro-symmetry (CS) parameter is applied in this study to distinguish the BCC and FCC phase.

Centro-symmetry parameter is first discussed by Kelchner et al [42], which is used to determine defects from the extensive elastic deformation in the thin film.

$$CS = \sum_{i=1}^{N/2} \left| \vec{R}_i + \vec{R}_{i+N/2} \right|^2 \quad (26)$$

As shown in Eq.26 [42], N is an input parameter and identifies how many nearest neighbors of each atom are found in ideal lattice. For example, in the FCC phase N is 12 but in the BCC phase N will change to 8. \mathbf{R}_i and $\mathbf{R}_{i+N/2}$ are vectors from the central atom to a particular pair of nearest neighbors. The N nearest neighbor vectors for each atom is first determined in an ideal bulk lattice with the orientation of the slab. According to the atom positions in the ideal lattice, the first group of $N/2$ nearest neighbor vectors (\mathbf{R}_i) from a center atom is generated by finding those neighbors in our simulation box with vectors closest in distance to the ideal nearest neighbor. Then the computer algorithm looks for the other groups of $N/2$ vectors ($\mathbf{R}_{i+N/2}$), which are on the centro-symmetry positions of the first group. Each pair of centro-symmetry (\mathbf{R}_i and $\mathbf{R}_{i+N/2}$) vectors will be added up and the centro-symmetry number CS is the sum of the squares of $N/2$ resulting vectors calculated [42]. In the ideal lattice each pair of centro-symmetry vector are equal and opposite, thus $\mathbf{R}_i + \mathbf{R}_{i+N/2}$ is equal to zero and cause the centro-symmetry number also equal to zero. In the real simulation box, however the atoms have thermal perturbations of a perfect lattice the centro-symmetry number will be a small positive number in a unity phase cell.

In this research, the number of nearest neighbors is fixed in the FCC phase ($N=12$). Therefore, the centro-symmetry will be small if the atom lies in the FCC phase. The BCC phase also have the centro-symmetry property, but since we check 12 neighbors, only four pairs of these atoms in the BCC phase match their centro-symmetry positions. The centro-symmetry number for atoms in the BCC phase will be larger than those in the FCC phase. Finally, since the atom sitting on the interface have no centro-symmetry property; these atoms will have the largest centro-symmetry numbers. Figure 29 shows an example of a centro-symmetry number profile for the 1400K simple. Using the centro-symmetry method, we determine the atoms with the CS number from 3.7 to 5.9 to be in the BCC

phase. The atom with a CS number lower than 3.7 is in the FCC phase. And all other atoms with a CS number greater than 5.9 are identified as interface atoms.

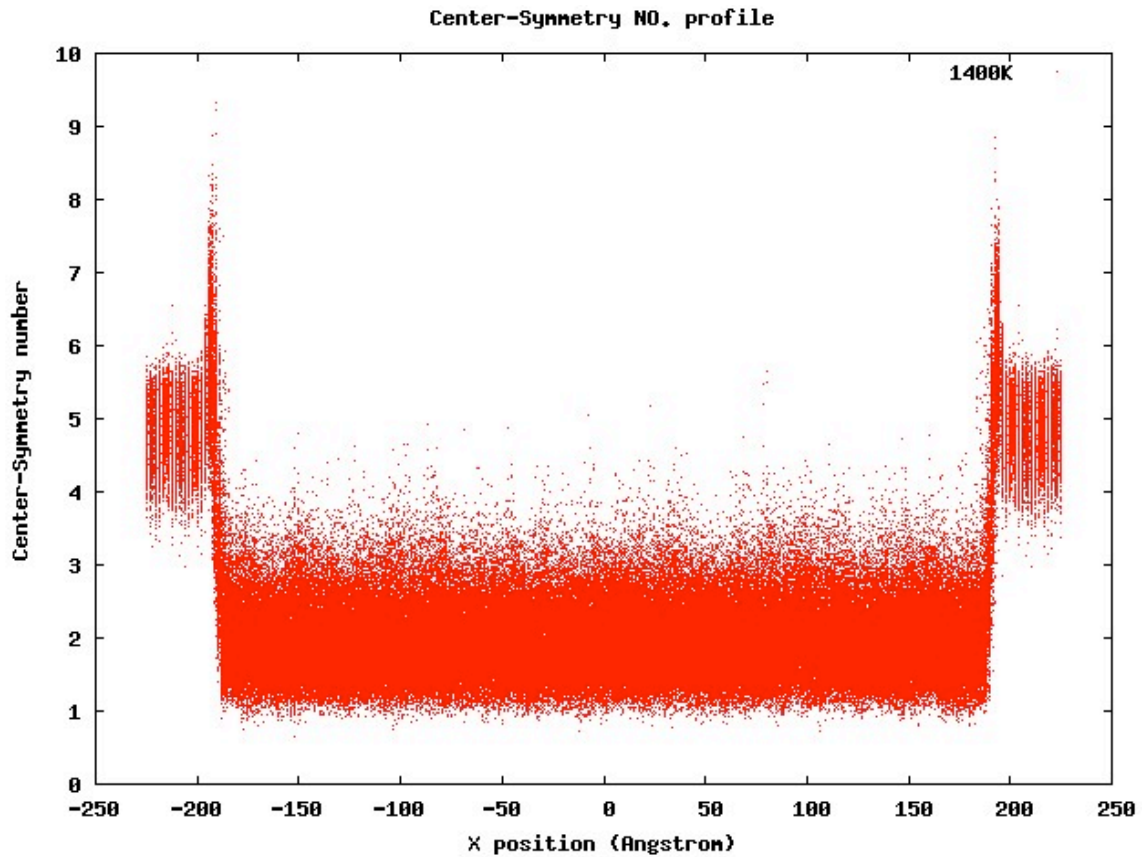


Figure 29

The centro-symmetry number (CS) profile for the 1400K simple. Each dot in the figure presents an atom in the simulation box. The x-axis locates the x position of atoms in units of angstrom. y-axis is the CS number of each atom. Two sides of the box are the BCC phases, which has a CS number from 3.7 to 5.9. The middle part is the FCC phase with a CS number lower than 3.7. All the atoms with a CS number greater than 5.9 are identified on the interface.

6.2 Planar interface growth and step ledge growth

Some previous studies of the solidification processes show that the solid phase grows in a plane structure. One of the examples is the solidification of Silicon (Si) along the faceted $\langle 111 \rangle$ direction. During the solidification, the solid Si will first nucleates in certain faceted terrace interface orientation like (111) plane. Then, once the nucleus become larger than the critical size, it will start to grow in a dish shape. Mostly, these nucleus dishes would have one atomic height and grow in a great speed though the whole interface. After the first nucleus dish fills the whole interface plane, the second plane layer will start to nucleate and grow on the first plane according to the same method [Un published research by Hoyt]. We call it planar structure growth. This layer-by-layer growing process is also observed in Bos's et al [33] martensitic transformation. Bos's et al. described that before the transformation started, the interface atomic plane had to build a screw dislocation network for the transformation to go through the entire interface plane. This screw dislocation network is a nucleus for the solid-solid interface. Similar to the Si solidification process, after the first layer of FCC plane completely transforms to the BCC phase, the screw network will start to build up and transform the next layer and so on. In our research, the interface also exhibits a planar structure growth property. As shown in Figure 21, the three ledges structure in the FCC phase separates the interface into three disconnections. During the transform, the interface remains fairly planar. Even though there are small fluctuation in the positions of the step in the X-direction, a large convex is not observed. In addition, where the BCC phase nucleates in the FCC phase and how the BCC steps grow are the questions that will be analyzed next.

One of possible mechanisms is the step ledge growth, which is described by Howe et al [43]. According to their experimental observation using transmission electron microscopy on several examples of FCC to BCC phase transformations. They found that the disconnection ledges could grow in the Burgers vector direction and cause the movement of the FCC-BCC interface. As introduced in Section 2.2.2, the Burgers vector

can be simply expressed as $\mathbf{b} = \mathbf{l}_\alpha + \mathbf{l}_\beta$ (Eq.5) in a homogeneous boundary. Figure 30 shows an example of a single step disconnection structure. If the λ and μ phases are in the same interface orientation, it is considered as a homogeneous boundary. Thus, the Burgers vector of the disconnection is the sum of the defect translation vectors in each phase. However, if the λ and μ phases are in a different interface orientation, Eq.5 has to be extended to form:

$$\mathbf{b} = -(\vec{t}_\lambda + P_{coh} \vec{t}_\mu) \quad (27)$$

In Eq.27, the \mathbf{t}_λ and \mathbf{t}_μ are the translation vectors in their own coordinate orientation, which are the vectors along the Burgers circuit in each phase. P_{coh} is a coherence matrix to convert a μ vector into the λ coordinate frame. Therefore, the Burgers vectors also can be estimated in a boundary of arbitrary orientation.

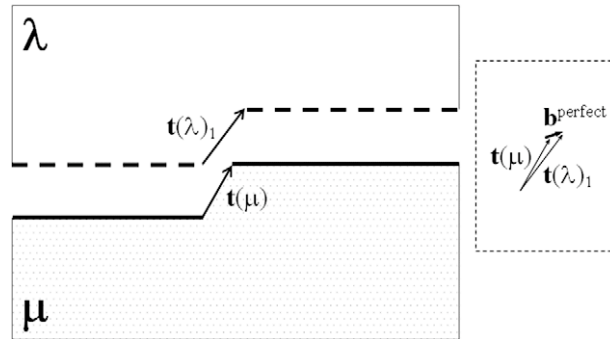


Figure 30 [43]

Schematic illustration of a single step disconnection cause by bonding misfit surface ledges on the λ and μ phases. If the λ - μ interface on the left side of the defect are bonded first, there must be a gap on the right side due to the difference of the translation vector in each phases. The perfect Burgers vector for the disconnection is the sum of the translation vector in λ and μ phases.

In the dislocation defect, the Burgers vector is the gliding direction for the dislocation under an external stress. During dislocation motion, a half plane of atoms is slipped in response to shear stress by the breaking and reforming of a line of bonds, one (or a few) at a time. The energy required to break a single bond, which is in the Burgers vector direction is far less than that to break all the bonds on an entire plane of atoms at once [44]. Similarly, the disconnection also prefers to glide or grow following its Burgers

vector. Since this direction requires low energy to break and rebuild the bond. Figure 31 is a high resolution TEM image showing an example of a disconnection in Au [45 & 46]. Based on Eq.27, the Burgers vector is calculated as shown in Figure 31. The coherent terraces can extend in the Burgers vector direction during the growth of the μ phase. In this way, the whole λ - μ interface moves in the direction of the vector α (Figure 31).

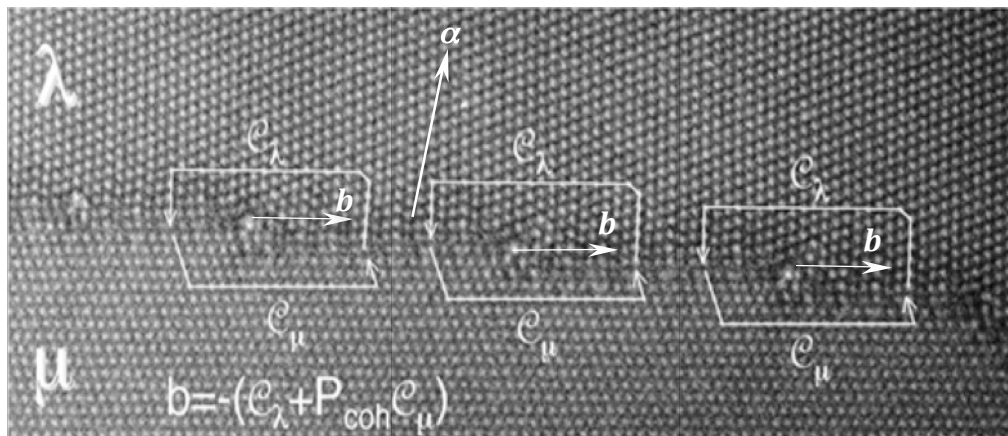


Figure 31 [45], [46]

A HRTEM image showing interfacial disconnections. Base on Equation 23, the Burgers vector is calculated directing as showing in the figure. Each disconnection steps can glide and grow following their Burgers vector direction. The net effect causes the transforming of the λ - μ interface to the α vector direction.

However, this step ledge growth phenomenon is not applicable in our interphase boundary setting. As shown in Figure 32, our α - γ boundary is an incoherent interface [47]. Since the BCC phase is a perfect single crystal without any defect, its defect translation vectors is equal to zero. On the other hand, the FCC phase is set up with three ledges structure, which has a defect translation vector t_{FCC} . Therefore, according to Eq. 27 the Burgers vector for the disconnection is equal to the $-t_{FCC}$ ($-b_p = t_{FCC} + P_{coh} \times 0$), which has a 66.5° angle with the BCC interface plane. Even though the disconnection still transforms along the Burgers vector (Figure 21), because of the angle between the Burgers vector and the interface, disconnection terraces cannot grow along its habit plane

direction. Thus, another kind of interface growing mechanics is required to support the plane structure growing behavior.

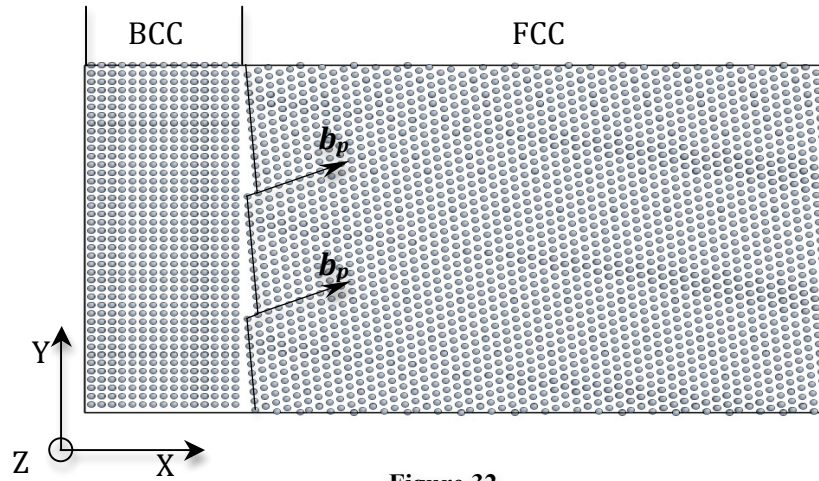


Figure 32

2-D side view of the simulation box setting. BCC phase is a perfect single crystal without defect. FCC phase has three ledges defect on the x-direction surfaces. According to Eq.27, the disconnection structure has burger b_p as showing in the figure.

6.3 Planar secondary disconnection growth

In the following we will refer to the disconnection structures of Figure 32 on the interface as the “primary disconnections”, with the vector b_p . Since the Burgers vector of the primary disconnection has a 66.5° tilt from the BCC habit plane, the growth of the primary disconnection cannot be parallel to the planar direction. However, the processing of the transformation still exhibits planar growth behavior (Figure 21). Therefore, more studies should focus on the atomistic phenomenon in the disconnection terrace plane.

6.3.1 Misfit dislocation in the terrace plane

Based on the simulation box geometry, the lattice parameter difference between the FCC and BCC phases forms periodic misfit dislocations on the interface. Table 7 lists the real lattice spacing in each orientation for the FCC and BCC phases. The normal view of

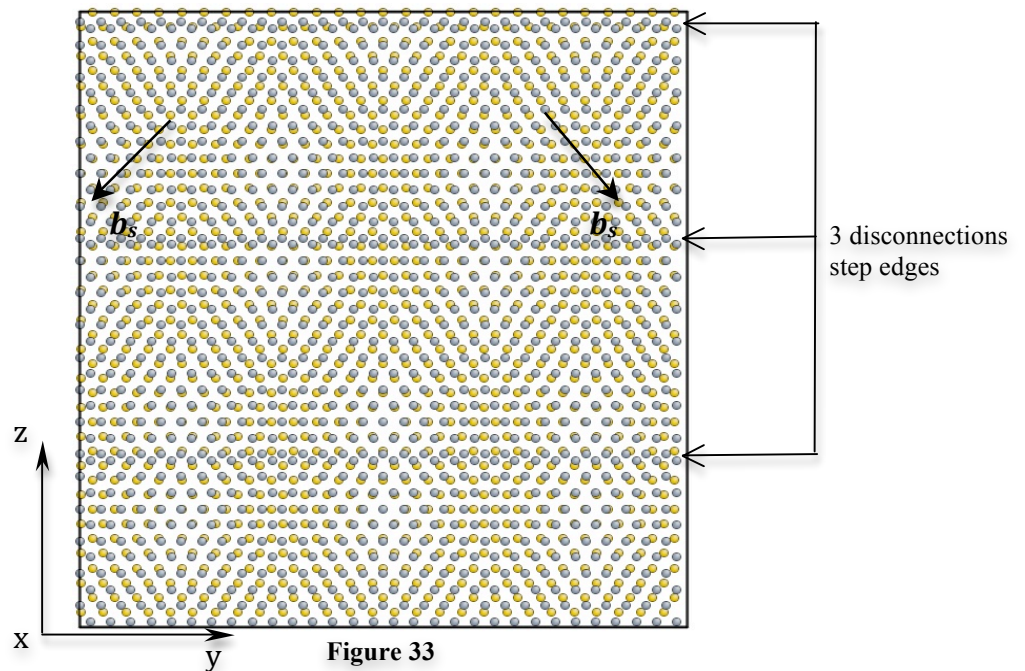
Spacing Temp (K)	FCC (Unit Å)			BCC (Unit Å)		
	X (7 7 6)	Y (3 3 -7)	Z (-1 1 0)	X (1 1 0)	Y (-1 1 0)	Z (0 0 1)
600	6.3721	5.8575	5.2158	4.0773	4.0773	2.8853
800	6.3782	5.8631	5.2208	4.0855	4.0855	2.8882
1000	6.3834	5.8678	5.2250	4.0930	4.0930	2.8942
1200	6.3911	5.8750	5.2313	4.1034	4.1034	2.9015
1400	6.3990	5.8822	5.2378	4.1112	4.1112	2.9070

Table 7

The real lattice spacing in each orientation for the FCC and BCC phases.

Figure 32 shows the ideal initial state of the α - γ interface, which assumes that all the atoms are located on their ideal lattice. In Figure 33, only two layers of the interface atoms are shown. The gray atoms belong to the FCC phase and the yellow atoms are in the BCC phase. As we mentioned in section 2.6, with the N-W close-packed interface

relationship, only 8% of the atoms can be considered as coherent in a flat plane interface. The coherent atoms were found to be grouped into small rhombic regions as shown in Figure 6 (a). Based on our interface geometry, our close-packed relationship relates to the N-W relationship and has the similar rhombic coherent region. Meanwhile, the 3 primary disconnection steps in the FCC phase raise the proportion of coherent atoms to around 25% by increase the frequency of repetition of the rhombic coherent regions (Figure 33). Moreover, according to the lattice spacing difference between the two phases on the interface plane (Table 7), the Burgers vector direction of these misfit dislocations are calculated to be around 37° tilt from the $(-1\ 1\ 0)$ direction of the BCC orientation, which



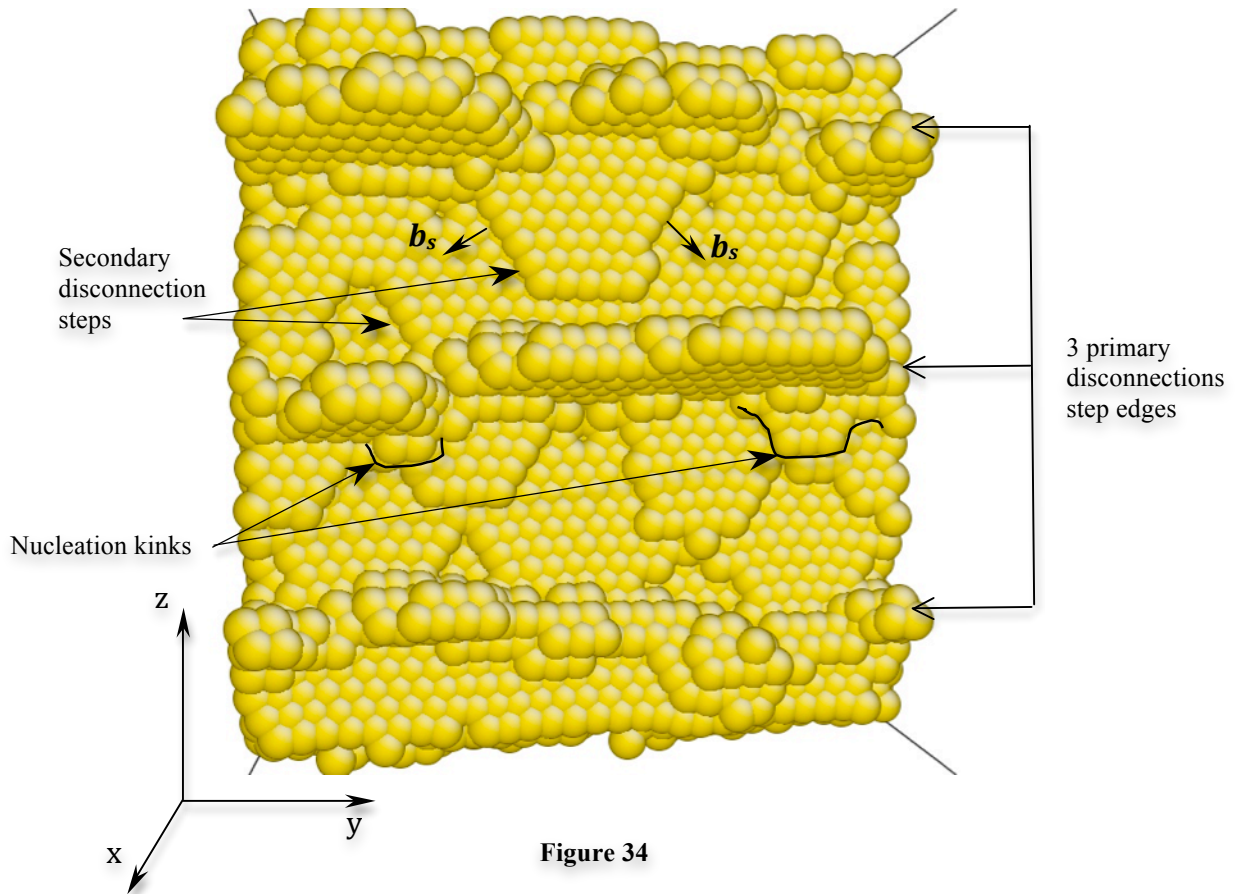
Cross section view normal to the interface in the ideal initial state. The gray atoms identify the FCC phase and the yellow atoms are in the BCC phase. Three disconnection steps separate the whole interface into three terrace plans. The rhombic area in each terrace plane is the atom matching area in each terrace. The misfit dislocation local in the interspaces between the rhombic area and the Burgers vectors (\mathbf{b}_s) is around 37° tilt from the $(-1\ 1\ 0)$ direction of the BCC orientation.

are shown as the vector \mathbf{b}_s in Figure 33. These misfit dislocations locate on the interspaces between two adjacent coherent rhombic areas in each terrace plane and extend to the step edge of the primary disconnection.

6.3.2 Secondary disconnection formation and growth in terrace plane

As we mentioned in the pervious chapter, the misfit dislocation caused by the lattice spacing difference between the FCC and BCC phase creates an interatomic stress. In order to release this stress, the terrace plans form another disconnection structure. Compared with the primary disconnection, which is created on the FCC – BCC interface, we call the disconnection located on each terrace plane to be “secondary disconnections”.

Figure 34 is a cross-section view of the simulation box, which is normal to the interface and only depicts the atoms belong to the BCC phase. As shown in Figure 34, three primary disconnections are gliding into the FCC phase follow along with their Burgers vector b_p . Some small kinks structures are forming around the primary disconnections step edges. It shows that the new BCC crystals prefer to nucleate on these primary disconnections steps edges. In addition, secondary disconnection structures can be observed in each terrace planes. These secondary disconnections have the Burgers vectors, which are identical as the misfit dislocations in the initial state. During the transformation, the kinks first nucleate on the primary disconnections steps edges, and then start to grow in a plane shape, forming the secondary disconnections. These secondary disconnections will extend along with their Burgers vectors until they fill in the whole terrace plane. Two to three secondary disconnections can arise at the same time in the same terrace plane but growth follows the plane order, which means the second secondary disconnections grows only when the secondary disconnections completely cover the whole terrace plane. Furthermore, the Burgers vectors of the secondary disconnection lay on the BCC habit plane. Therefore, the secondary disconnection steps have a plane growing behavior, which is parallel to the BCC habit plane. Thus, this secondary disconnection growth mechanic not only explains why the interface still shows plane growing behavior, even though the primary disconnections have a 66.5° tilt from the BCC habit plane, but also validates the disconnection growth theory introduced in previous investigations.



3D – cross section view of the interface during the transformation with only the BCC atoms indicated. There are kinks nucleated on the edge of the primary disconnection steps. Several secondary disconnection are growing in their Burgers vectors direction in each terrace plane.

6.4 Analysis and discussion

According to an observation of interface snapshots during the transformation, the transformation mechanics become more intelligible. The step edges of the primary disconnection create a heterogeneous site to allow the BCC crystal to nucleate on the interface. Most of the nuclei will shrink and disappear once they nucleate. Only the nuclei that are greater than the critical size will grow as a kink on the primary disconnection step edge. Then the kinks try to form a secondary disconnection structure in each terrace planes to release the interatomic stress that are created by the misfit dislocations on the BCC-FCC interphase boundary. After that, the secondary disconnections grow in their Burgers vectors direction, which is parallel to the BCC habit plane and go through the whole terrace plane.

In order to further analyze the nucleation and transformation process, a microscopic potential energy profile is zoomed into one atomic plane level. At the initial snapshot, one side of the interface is located at -192.21 in the x-axis. Two individual observing windows are opened at $-76.5\text{\AA} \sim -74.3\text{\AA}$ and $-65.7\text{\AA} \sim -63.7\text{\AA}$ in the x-axis, which are parallel to the FCC-BCC interface. Each window only contains one plane of atoms. Figure 35 is a potential energy versus time of these two layers of atoms as the interface passes by. Layer 1 is located on X-position $-76.5\text{\AA} \sim -74.3\text{\AA}$, which is closer to the interface than the Layer 2 at $-65.7\text{\AA} \sim -63.7\text{\AA}$. When the interface approaches, the atoms will vibrate more and more strongly and depart from their original lattice position (FCC), which causes an increase of potential energy (Figure 35). At the same time, the BCC kinks nucleate and shrink on the primary disconnection edges. Once their potential energy crosses the activation energy, the kinks start to grow in the plane shape following the direction of secondary disconnection Burgers vectors. Then the potential energy decreases during the planar transformation. The three jumps in each layer's energy profile identify the complete transformation of the three terrace planes in the interface. These potential energy jumps show a partial independent transformation behavior in each

terrace plane that means the transformation can occur on each terrace in different time and one terrace can grow surpass or behind to another. This partial independent transformation also explains the alternation between concave and convex structures of the interface during the transformation.

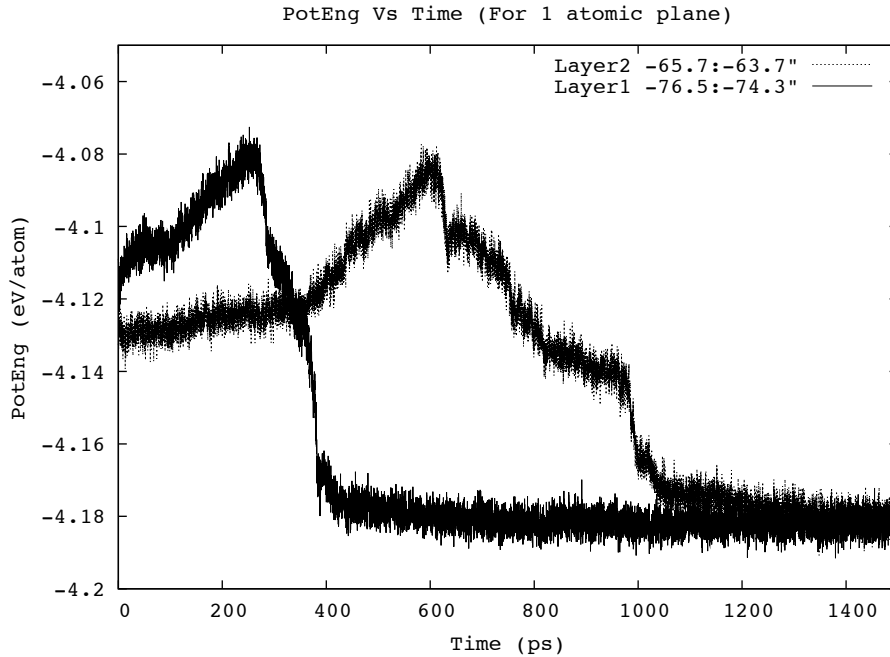


Figure 35

A potential energy profile of two individual layers of atoms. Each layer only contains 1 plane of atoms, which is parallel to the FCC-BCC interface. Layer 1 locate on x-position $-76.5\text{\AA} \sim -74.3\text{\AA}$ and Layer 2 is at $-65.7\text{\AA} \sim -63.7\text{\AA}$.

However, the growing difference between each terrace plane is less than 3 atom planes (Figure 21), otherwise the interface will slow down to wait for the trailing terrace plane. Thus, the interface speed is non-uniform during the transformation, which can be reflected as the nonlinear decrease of the potential energy in the total potential graph (Figure 22-26). Combining with the fluctuation effect, the transformation speed for each plane can be significantly different (Figure 35). After the transformation, the potential energy equilibrates to the BCC phase level.

6.5 Summary

By means of molecular dynamic method and computational simulation techniques, the interface growth mechanism during the γ - α massive transformation is found. Based on our analysis, the primary disconnection is acting as seedbed to create a heterogeneous site to let the BCC kinks nucleate. The BCC kinks prefer to form a secondary disconnection in each terrace plane to release the dislocation stress caused by the mismatch of FCC and BCC lattice. Once the atoms gain enough energy to cross the activation energy barrier, the BCC kinks will grow in a plane shape following the directions of the secondary disconnection burgers vectors. During the transformation, the interfaces show a partial independent transformation behavior in each terrace plane and cause a non-uniform moving speed of the interfaces (Figure 22-26), which is more obvious in the low temperature cases. Since the massive transformation avoids the diffusion effect of the solute drag, its transformation speed shows a strong nucleation rate dependent. Future research can focus on the nucleation step and the effect of the driving force to the nucleation to further explain how the transformation speed relates to temperature.

Chapter 7

Future research

With the successful setting of the basic model to simulate the austenite – ferrite transformation in pure iron, further research can be approached.

1. Some previous researches on the γ - α transformation have suggested a strong interface orientation dependence. Thus, new interface close-pack relationships can be tested like the N-W and K-S relationship, to check the transformation behavior under different lattice orientations.
2. As discussed in Section 6.3, the transformation follows a planar secondary disconnection growth mechanism and the BCC kinks nucleate on the primary step edge. Therefore, on one hand, changing the number of steps will directly affect the BCC nucleation rate. On the other hand, adjusting in the length of each ledge should change the speed of the planar secondary disconnection growth. Both ways will influence the interface velocity and mobility under the same temperature and driving force condition. Thus, a future study can focus on the effect of the primary and secondary disconnection structure to the transformation.
3. Since the MD cannot simulate the iron magnetic effect, the driving force based on the Ackland et al. 1997 potential does not represent the real circumstance accurately. However, in MD simulations, the driving force can be adjusted based on experimental values by adding potential energy to one of the phases (FCC or BCC) in the system. Therefore, new observations can use the experimental driving force to compare the results between the simulation and experiment, and analyze the significant activation energy difference between them.

4. Impure atoms like Cu, Mn, C can be added in the system as solute drag elements. Even though, during the massive transformation, the interface moves so fast that no diffusion should be observed during the transformation, the effect of these impure atoms are still worth studying to further research the massive transformation behavior in the alloy system.
5. During this research, all the observations are based on a single crystal FCC – BCC simulation setting. Future studies can extend the system and create a multi-crystal simulation box to study the influence between the grain boundaries and improve the authenticity of the simulation.

Chapter 8

Conclusion

In summary, Austenite(γ) to Ferrite(α) massive transformation for pure iron has been studied using MD simulation based on the Ackland et al. 1997 iron alloy potential. A method to determine the grain boundary velocity and mobility during the transformation has been demonstrated. The interphase boundary uses a close-pack orientation, which is 4.04° tilted in Z-direction $[-1\ 1\ 0]$ plane of the FCC box based on the N-W relationship. In this way, two kinds of disconnection structures are created. The primary disconnection created by the tilting interface geometry establishes heterogeneous sites to allow the BCC crystal to nucleate on the interface. Moreover, because of the incoherence of the FCC – BCC interface, there are misfit dislocation located on the interface in the initial moment. Thus, secondary disconnections form in each terrace plane to release the stress created by those dislocations. During the transformation, the kinks nucleating on the step edge of the primary disconnection will grow in the Burgers vector direction of the secondary disconnections in each terrace plane. The secondary disconnections glide through the whole terrace plane and show a strong planar growth mechanism.

According to the potential energy profile during the transformation. The interface velocity and mobility obtained in five simulation with temperature range 600 K to 1400 K, are around 2 m/s and $10e-03\ \text{m}^*\text{mol}/\text{J}\cdot\text{s}$. The activation energy calculated based on this result is 16kJ/mole, which is much lower than the experimental value. Therefore, based on our models, further research will focus on multi-crystal structure and adding solute drag impurities to the system to explain the variance between the simulation value and the experimental.

Appendix A

Classical Mechanics of MD simulation

Newton's equation of motion is given by

$$F_i = m_i a_i \quad (\text{A.1})$$

where F_i is the force exerted on particle i , m_i is the mass of particle i and a_i is the acceleration of particle i . The force can also be expressed as the gradient of the potential energy,

$$F_i = -\nabla_i U \quad (\text{A.2})$$

Combining these two equations yields

$$-\frac{dU}{dr_i} = m_i \frac{d^2 r_i}{dt^2} \quad (\text{A.3})$$

where U is the potential energy of the system. Newton's equation of motion can then relate the derivative of the potential energy to the changes in position as a function of time.

Newton's Second Law of motion: a simple application

$$F = m \cdot a = m \cdot \frac{dv}{dt} = m \cdot \frac{d^2 x}{dt^2} \quad (\text{A.4})$$

Taking the simple case where the acceleration is constant,

$$a = \frac{dv}{dt} \quad (\text{A.5})$$

we obtain an expression for the velocity after integration

$$v = at + v_0 \quad (\text{A.6})$$

and since

$$v = \frac{dx}{dt} \quad (\text{A.7})$$

we can once again integrate to obtain

$$x = v \cdot t + x_0 \quad (\text{A.8})$$

Combining this equation with the expression for the velocity, we obtain the following relation which gives the value of x at time t as a function of the acceleration, a the initial position, x_0 and the initial velocity v_0 .

$$x = a \cdot t^2 + v_0 \cdot t + x_0 \quad (\text{A.9})$$

The acceleration is given as the derivative of the potential energy with respect to the position r ,

$$a = -\frac{1}{m} \frac{dE}{dr} \quad (\text{A.10})$$

Therefore, to calculate a trajectory, one only needs the initial positions of the atoms, an initial distribution of velocities and the acceleration, which is determined by the gradient of the potential energy function. The equations of motion are deterministic, e.g., the positions and the velocities at time zero determine the positions and velocities at all other times t . The initial positions can be obtained from experimental structures, such as the x-ray crystal structure of the protein or the solution structure determined by NMR spectroscopy.

The initial distribution of velocities are usually determined from a random distribution with the magnitudes conforming to the required temperature and corrected so there is no overall momentum, i.e.,

$$P = \sum_{i=1}^N m_i v_i = 0 \quad (\text{A.11})$$

The velocities, v_i , are often chosen randomly from a Maxwell-Boltzmann or Gaussian distribution at a given temperature, which gives the probability that an atom i has a velocity v_x in the x direction at a temperature T .

$$P(v_{ix}) = \left(\frac{m_i}{2\pi k_B T} \right)^{1/2} \exp\left(-\frac{1}{2} \frac{m_i v_{ix}^2}{k_B T} \right) \quad (\text{A.12})$$

The temperature can be calculated from the velocities using the relation

$$T = \frac{1}{(3N)} \sum_{i=1}^N \frac{|P_i|}{2m_i} \quad (\text{A.13})$$

where N is the number of atoms in the system.

Appendix B

Ackland et al. 1997[15] EAM Finnis-Sinclair potential

In the framework of the Finnis-Sinclair formalism, the energy of an assembly of N atoms is given by

$$E_{tot} = \frac{1}{2} \sum_{i \neq j=1}^N V_{ij}(x_{ij}) - \sum_{i=1}^N \left(\sum_{j=1}^N \Phi_{ij}(x_{ij}) \right)^{1/2} \quad (\text{B.1})$$

in which V_{ij} identify the pairwise repulsive part of the potential and $\Phi(x_{ij})$ is the cohesive term also a pairwise function. The iron-iron potential was derived by the fitting method discuss by Ackland et al. 1987 [18], with fits to the lattice parameter a_0 , elastic constants C_{11} , C_{12} and C_{44} , and cohesive energy E_c of α -iron and an estimated unrelaxed vacancy formation energy of 1.89eV. Since the Finnis-Sinclair formalism cannot process the magnetic effect or changes in shape of the local electronic density of states. Thus, it does not reproduce the iron phase diagram quantitatively. Base on above input parameters, the model provide a stable BCC structure over the FCC in the whole temperature profile. However, the γ (FCC phase) iron can still be stabilized and equilibrated individually with the Ackland et al. 1997 potential. That is why Ackland et al. 1997 potential was chose in this project.

The Ackland et al. 1997 potential was first developed for simulating Fe-Cu alloy. Therefore, for a binary alloy system of atom species A and B, the potential function can be denoted V^{AA} , V^{BB} , V^{AB} , Φ^{AA} , Φ^{BB} and Φ^{AB} . However, in this project, we only use the Fe-Fe metallic bond data. For these parameterizations, the pairwise function and local density function can be expressed as:

$$V^{AA}(x) = \sum_{k=1}^m a_k^{AA} H(r_k^{AA} - x) (r_k^{AA} - x)^3 \quad (\text{B.2})$$

$$\Phi^{AA}(x) = \sum_{k=1}^2 A_k^{AA} H(R_k^{AA} - x) (R_k^{AA} - x)^3 \quad (\text{B.3})$$

In this notation, H is the Heaviside step function, and other parameters are list in the (Table B. 1).

	Fe-Fe	Cu-Cu	Fe-Cu
a_1	-36.559853	29.059214	0.855556
a_2	62.416005	-140.05681	-1.208212
a_3	-13.155649	130.07331	0.483162
a_4	-2.721376	-17.48135	0.925402
a_5	8.761986	31.82546	2.592094
a_6	100.0000	71.58749	5.000000
A_1	72.868366	9.806694	
A_2	-100.944815	16.774638	
r_1	1.180000	1.2247449	3.200000
r_2	1.150000	1.1547054	3.000000
r_3	1.080000	1.1180065	2.950000
r_4	0.990000	1.0000000	2.850000
r_5	0.930000	0.8660254	2.500000
r_6	0.866025	0.7071068	2.475000
R_1	1.300000	1.2247449	
R_2	1.200000	1.0000000	
a_0 (Å)	2.8665	3.615	

Table B. 1 [15]

Parameters for the many-body potentials for iron, copper and iron-copper. For pure metals they are given in units of eV a_0^{-3} , eV² a_0^{-3} , a0 and a_0 for a_k , A_k , r_k and R_k , respectively, whereas for the alloy lengths are in Å. (Ackland et al. 1997 [15])

Bibliography

1. M. Hillert, L. Höglund. *Mobility of a/c phase interfaces in Fe alloys*. Scripta Mater Vol. 54, pp.1259-1263 (2006)
2. G.P. Krielaart, J. Sietsma, Sybrand van der Zwaag. *Ferrite formation in Fe-C alloys during austenite decomposition under non-equilibrium interface conditions*. Material Science and Engineering, Vol. 237, pp.216-223. (1997)
3. Ashby, Michael F, David R. H. Jones. *Engineering Materials 2*. Oxford: Pergamon Press. ISBN 0-08-032532-7. (1992)
4. Y. van Leeuwen. *Moving Interphases in Low-Carbon Steel*. PhD dissertation, Delft University of Technology, Department of Materials Science and Engineering, (1998).
5. SJ. J Plimpton. *Computational Limits of Classical Molecular-Dynamics Simulations*. Computational Materials Science, Vol. 4, pp.361-364. (1995)
6. LAMMPS Molecular Dynamics Simulator:
<http://www.cs.sandia.gov/~sjplimp/lammps.html>.
7. M.S. Daw and M.I. Baskes. *Semiempirical, quantum mechanical calculation of hydrogen embrittlement in metals*. Physical Review Letters, Vol. 50:1285, (1983)
8. M.S. Daw and M.I. Baskes. *Embedded-atom method: Derivation and application to impurities, surfaces, and other defects in metals*. Physical Review B, Vol. 29:6443, (1984)
9. M.S. Daw, S.M. Foiles, M.I. Baskes. *The Embedded Atom Method: A review of theory and applications*. Mater Sci Rep, Vol. 9, pp.251-310. (1993)
10. M.W. Finnis and J.E. Sinclair, *A simple empirical N-body potential for transition-metals*. Philos. Mag, Vol.50, pp.45-56 (1984)

11. R.A. Johnson and D.J. Oh, *Analytic embedded atom method model for bcc metals*. Journal of Materials Research, Vol. 4(5), pp.1195-1201. (1989)
12. M.I. Mendeleev et al. *Development of new interatomic potentials appropriate for crystalline and liquid iron* Philos. Mag Vol.83, NO. 35, pp. 3977-3994 (2003)
13. H. M. Pak and M.Doyama, *J. Fac. Engng, Tokyo Univ., B*, Vol. 30, pp. 111. (1969)
14. Yu.N. Osetsky, A. G. Mikhn and A. Serra, *Study of copper precipitates in α -iron by computer simulation I. Interatomic potentials and properties of Fe and Cu*. Phil. Mag. A, Vol. 72, pp. 361. (1995)
15. G. J. Ackland, D. J. Bacon, A. F. Calder, and T. Harry, *Computer simulation of point defect properties in dilute Fe-Cu alloy using a many-body interatomic potential*. Phil. Mag, A, Vol.75, pp.713. (1997)
16. A.E. Carlsson, *Solid State Phys. Rev. Lett.* Vol.43, 1. (1990)
17. D.Y. Sun, M. Asta, J.J Hoyt, M.I. Mendeleev, and D.J. Srolovitz. *Crystal-melt interfacial free energies in metals: fcc versus bcc*. Physical Review B, Vol. 69 : 020102, (2004)
18. G.J. Ackland, G.I. Tichy, V. Vitek, and M.W. Finnis, *Simple N-body potentials for the noble metals and nickel*. Phil. Mag. A, Vol. 56, pp. 735. (1987)
19. J.P. Hirth, *Dislocations, steps and disconnections at interfaces*. J. Phys. Chem. Solids, Vol.55, pp.985-89. (1994)
20. R.C. Pond, *Dislocations in Solids* (Edited by F.R.N. Nabarro) Vol.8, p.1. North-Holland, Amsterdam (1989).
21. M.Hillert. *Diffusion and interface control of reactions in alloys*. Metall Trans, Vol.6A, pp.5-19. (1975)

22. G.P.Krielaart, S.Van Der Zwaag. *Kinetics of gamma->alpha phase transformation in Fe-Mn alloys containing low manganese*. Mater Sci Technol, Vol.14, pp.10. (1998)
23. J.J.Wits, T.A.Kop, Y.V.Leeuwen, J.Seitsma, S.Van Der Zwaag. *A study on the austenite-to-ferrite phase transformation in binary substitutional iron alloys*, Mater Sci Eng A, Vol.283:234. (2000)
24. S.I.Vooija, Y.V.Leeuwen, J.Seitsma, S.Van Der Zwaag. *On the Mobility of the Austenite-Ferrite Interface in Fe-Co and Fe-Cu*. Metall Mater Trans A, Vol.31:379. (2000)
25. G.R.Speich, R.L.Miller. *Temperaturing of ferrite-martensite steels*. Trans Metall Soc, AIME, Vol.245, pp.1063. (1969)
26. Y.C.Liu, F.Sommer, E.J.Mittemeijer. *Abnormal austenite-ferrite transformation behavior of pure iron*. Philos Mag, Vol.84, pp.1853. (2004)
27. Y.C.Liu, F.Sommer, E.J.Mittemeijer. *Kinetics of the abnormal austenite-ferrite transformation behaviour in substitutional Fe-based alloys*. Acta Mater. Vol.52, pp.2549-2560. (2004)
28. F.W.Jones, W.I.Pumphrey, *Free Energy and Metastable States in the Iron-Nickel and Iron-Manganese Systems*. J Iron Steel Inst, Vol.163, pp.121. (1949)
29. G.P.Krielaart, J.Seitsma, S.Van Der Zwaag. *Ferrite formation in Fe-C alloys during austenite decomposition under non-equilibrium interface conditions*. Mater Sci Eng A, Vol.237, pp.216-223. (1997)
30. J.M. Rigsbee, H.I. Aaronson *A computer modeling study of partially coherent FCC:BCC boundaries*. Acta Metallurgica. Vol. 27, pp. 351-363 (1979)

31. J.H.van der Merwe, G.J.Shiflet. *Role of structural ledges at phase boundaries- III. F.C.C.-B.C.C. interfaces in Kurdjumov-Sachs orientation*. Acta Mater. Vol.42, No.4, pp.1199-1205, (1994)
32. M.G.Hall, H.I.Aaronson and K.R.Kinsman. *Carbon content of small regions of austenite and transformation mechanism of Mo₂C fibres*. Iron and Steel Institute. Vol.210, pp. 541, (1972)
33. C. Bos, J. Sietsma, B. J. Thijsse. *Molecular dynamics simulation of interphase dynamics during the fcc-bcc transformation of a martensitic nature*. Phys Rev B, Vol.73, 104117 (2006).
34. J.J.Hoyt, D.Olmsted, S.Jindal, M.Asta, A.Karma. *Method for Computing Short-Range Forces between Solid-Liquid Interphases driving Grain Boundary Premelting*. Phys. Rev. E 79. 020601. (2009)
35. J.R.Morris and X.Song. *The melting lines of model systems calculated from coexistence simulations*. Chem Phys. Vol. 116, No. 21. (2002)
36. David R. Gaskell. *Introduction to the Thermodynamics of Materials*. 4th Ed. Great Britain: Taylor & Francis, (2003)
37. R.C. Pond, S. Celotto, J.P. Hirth. *A comparison of the phenomenological theory of martensitic transformations with a model based on interfacial defects*. Acta Mater. Vol. 51, 5385-5398. (2003)
38. J.W. Christian. *The Theory of Transformations in Metals and Alloys 2nd ed.* Oxford ; New York : Pergamon Press, (1975)
39. John Edward Lennard-Jones. *On the Determination of Molecular Fields. I. From the Variation of the Viscosity of a Gas with Temperature*. Royal Society of London. Series A, Containing Papers of a Mathematical and Physical Character 106 pp. 441-462 (1924)
40. Chris Swain. *Drug Discovery Resources*. Cambridge Medchem Consulting. 7 June (2010)

41. Y. van Leeuwen, T.A. Kop, J. Sietsma and S. van der Zwaag. *Phase transformations in low-carbon steels ; modelling the kinetics in terms of the interphase mobility*. J. Phys. IV France. Vol. 09, pp. 401-409 (1999).
42. C. L. Kelchner, S. J. Plimpton, J. C. Hamilton, *Dislocation nucleation and defect structure during surface indentation*. Phys Rev B, 58, 11085 (1998).
43. J.M. Howe, R.C. Pond, J.P. Hirth, *The role of disconnection in phase transformations*. Progress in Materials Science, Vol. 54, pp. 792-838 (2009).
44. D.J. Bacon, D. Hull, *Introduction to Dislocations*. Pergamon Press, 3rd Edition (1984).
45. D.L. Medlin, D. Cohen, R.C. Pond, *Accommodation of coherency strain by interfacial disconnections at a $90^\circ <110>$ grain boundary in gold*, Philosophical Magazine Letters, Vol. 83 (4), p.p. 223 (2003).
46. R.C. Pond, D.L. Medlin, and A. Serra, *A study of the accommodation of coherency strain by interfacial defects at a grain boundary in gold*, Philos. Mag. Vol. 86, p.p. 29-31 (2006).
47. J.M. Howe, H.I. Aaronson and J.P. Hirth, *Aspects of interphase boundary structure in diffusional phase transformations*. Acta Materialia, Vol. 48, p.p 3977-3984, (2000).
48. A.N. Kolmogorov presented by Mirkin LL. Sbornik Trudov Moskoskogo Instituta Stali, No.10, 1938.
49. D.A. Molodov, U. Czubayko, G. Gottstein, L.S. Shvindlerman, *On the effect of purity and orientation on grain boundary motion*. Acta Materialia, Vol. 46, n 2, p.p. 553-64, (1998).
50. SM. Foiles, J.J. Hoyt, *Computation of grain boundary stiffness and mobility from boundary fluctuations*. Acta Materialia, Vol.54, n1, pp.3351-3357 (2006).

51. D.A. Molodov, U. Czubyko, G. Gottstein, L.S. Shvindlerman, *On the effect of purity and orientation on grain boundary motion*. Acta Materialia, Vol. 46, n 2, p.p. 553-64, (1998).
52. Y.C.Liu, F.Sommer, E.J.Mittemeijer. *Abnormal austenite-ferrite transformation behavior of pure iron*. Philos Mag, Vol.84, pp.1853. (2004)
53. J.W. Rutter, K.T. Aust, Trans. AIME, 215, 119 (1959)
54. M. Winning, A.D. Rollett. *Transition between low and high angle grain boundaries*. Acta Materialia, Vol. 53, p.p. 2901-2907, (2005)